Glueball spectrum and matrix elements on anisotropic lattices

Y. Chen,[1,2] A. Alexandru,[2] S. J. Dong,[2] T. Draper,[2] I. Horváth,[2] F. X. Lee,[3,4] K. F. Liu,[2] N. Mathur,[2,4] C. Morningstar,[5] M. Peardon,[6] S. Tamhankar,[2] B. L. Young,[7] and J. B. Zhang[8]

[1]*Institute of High Energy Physics, Chinese Academy of Sciences, Beijing 100049, People's Republic of China*
[2]*Department of Physics & Astronomy, University of Kentucky, Lexington, Kentucky 40506, USA*
[3]*Center for Nuclear Studies, Department of Physics, George Washington University, Washington, D.C. 20052 USA*
[4]*Jefferson Lab, 12000 Jefferson Avenue, Newport News, Virginia 23606, USA*
[5]*Department of Physics, Carnegie Mellon University, Pittsburgh, Pennsylvania 15213, USA*
[6]*School of Mathematics, Trinity College, Dublin, Dublin 2, Ireland*
[7]*Department of Physics and Astronomy, Iowa State University, Ames, Iowa 50011, USA*
[8]*CSSM and Department of Physics, University of Adelaide, Adelaide, SA 5005, Australia*
(Received 13 October 2005; published 26 January 2006)

The glueball-to-vacuum matrix elements of local gluonic operators in scalar, tensor, and pseudoscalar channels are investigated numerically on several anisotropic lattices with the spatial lattice spacing ranging from 0.1–0.2 fm. These matrix elements are needed to predict the glueball branching ratios in J/ψ radiative decays which will help identify the glueball states in experiments. Two types of improved local gluonic operators are constructed for a self-consistent check and the finite-volume effects are studied. We find that lattice spacing dependence of our results is very weak and the continuum limits are reliably extrapolated, as a result of improvement of the lattice gauge action and local operators. We also give updated glueball masses with various quantum numbers.

DOI: 10.1103/PhysRevD.73.014516 PACS numbers: 12.38.Gc, 11.15.Ha, 12.39.Mk

I. INTRODUCTION

Glueballs, predicted by QCD, are so exotic from the point of view of naive quark model that their existence will be a direct support of QCD. However, experimental efforts in searching for glueballs are confronted with the difficulty of identifying glueballs unambiguously, even though there are several candidate glueball resonances, such as $f_0(1370)$, $f_0(1500)$, $f_0(1710)$, and $f_J(2220)$, etc. The key problem is that there is little knowledge of the nature of glueballs and confined QCD vacuum, which requires reliable nonperturbative methods to be implemented. The numerical study of lattice QCD, which starts from the first principles, has been playing an important role in this hot field in the last 20 years, and extensive numerical studies have been carried out to calculate the glueball spectrum [1–4]. These studies give the result that the masses of the lowest-lying glueballs range from 1 to 3 GeV, and suggest that the J/ψ radiative decays be an ideal hunting ground for glueballs. However, apart from the mass spectrum, more characteristics are desired in order to determine glueballs in the final states of J/ψ radiative decays, one of which is the partial widths of J/ψ decaying into glueballs. The first step to estimate these partial widths is to calculate the vacuum-to-glueball transition matrix elements (TME) of local gluonic operators, which are nonperturbative quantities and can be investigated by the numerical calculation of lattice gauge theory.

Glueball transition matrix elements were calculated first in $SU(2)$ [5] and $SU(3)$ [6,7] gauge theories with Wilson gauge action on isotropic lattice. In the calculation of glueballs, it is known that very large statistics are necessary in order for the correlation functions of gluonic operators to be measured precisely by Monte Carlo simulation. This prohibits the lattice size being too large. On the other hand, because of the large masses of glueballs, the lattice spacing (at least in the temporal direction) has to be small enough so that reliable signals can be measured before they are undermined by statistical fluctuations. This dilemma is circumvented by using anisotropic lattices, which are spatially coarse and temporally fine. The potentially large lattice artifacts owing to the spatially coarse lattice can be suppressed by the implementation of improved lattice gauge actions. Morningstar and Peardon applied these techniques to the calculation of glueball spectrum for the first time [4]. This treatment is verified to be successful and is thus adopted as the basic formalism of this work.

The glueball matrix elements computed in this work are of the form $\langle 0|g^2 \mathrm{Tr} G_{\mu\nu} G_{\rho\sigma}(x)|G\rangle$, where $|G\rangle$ refers to the glueball state with specific quantum number $J^{PC} = 0^{++}$, 2^{++}, or 0^{-+}, $G_{\mu\nu}(x)$ is the gauge field strength, and g the gauge coupling. The lattice version of the gluonic operators $g^2 \mathrm{Tr} G_{\mu\nu} G_{\rho\sigma}(x)$ are constructed by the smallest Wilson loops on the lattice. To reduce lattice artifacts, the lattice version of each local gluonic operator is improved by eliminating the $O(a_s^2)$ (a_s here is the spatial lattice spacing), while the glueball states $|G\rangle$ are obtained by smeared gluonic operators. In order to get a reliable continuum extrapolation, five independent calculations are carried out on lattices with spatial lattice spacings ranging from 0.09 to 0.22 fm. As by-products, we also calculate the masses of the lowest-lying stationary states in all of the symmetry channels allowed on a cubic lattice at each lattice spacing. To study the systematic error from finite

volume, two extra independent studies are performed at $\beta = 2.4$ with the same input parameters but different lattice size. Note that the local operators mentioned above are all bare operators, they need to be renormalized to give the physical matrix elements. In this work, the renormalization constants of the scalar and tensor gluonic operators at the largest lattice spacing are extracted by the calculations of gluonic three-point functions on a much larger statistical sample (100 000 measurements). The pseudoscalar operator renormalization is determined through the calculation of the topological susceptibility. Finally, we give the nonperturbatively calculated and phenomenologically significant matrix elements.

This paper is organized as follows. We give a detailed description of the construction of lattice local gluonic operators in Sec. II, where two types of lattice realization in each channel are defined. In Sec. III are the details of the computation, such as the generation of gauge configurations, the determination of lattice spacings, the construction of the smeared glueball correlators, the extraction of glueball masses and matrix elements, as well as the discussion of the finite volume effects and the continuum-limit extrapolation. Section IV is devoted to the nonperturbative renormalization of the local gluonic operators. The final results of glueball matrix elements and their physical implications are discussed in Sec. V. Section VI gives the conclusion of this work.

II. LOCAL GLUONIC OPERATORS AND MATRIX ELEMENTS

In the continuum theory, the lowest-dimensional gauge invariant gluonic operators are of the form $g^2 \mathrm{Tr} G_{\mu\nu} G_{\rho\sigma}$, of which the most commonly studied ones are the scalar $S(x)$ (QCD trace anomaly), the pseudoscalar $P(x)$ (topological charge density), and the tensor $\Theta_{\mu\nu}(x)$ (energy-momentum density). They all have dimension four and are all positive under charge conjugation. The explicit forms of them are

$$\begin{aligned} S(x) &= g^2 \mathrm{Tr} G_{\mu\nu}(x) G_{\mu\nu}(x), \\ P(x) &= g^2 \epsilon_{\mu\nu\rho\sigma} \mathrm{Tr} G_{\mu\nu}(x) G_{\rho\sigma}(x), \\ \Theta_{\mu\nu}(x) &= 2 g^2 \mathrm{Tr}(G_{\mu\alpha}(x) G_{\alpha\nu}(x) - \tfrac{1}{4} \delta_{\mu\nu} G^2(x)). \end{aligned} \tag{1}$$

If we introduce the chromoelectric and chromomagnetic fields,

$$E_i = G_{i0} \quad \text{and} \quad B_i = -\tfrac{1}{2} \epsilon_{ijk} G_{jk}, \tag{2}$$

the Lorentz scalar $S(x)$ and pseudoscalar $P(x)$ can be expressed explicitly by these operators,

$$\begin{aligned} S(x) &= 2 g^2 \mathrm{Tr}(\mathbf{B}(x)^2 + \mathbf{E}(x)^2), \\ P(x) &= 8 g^2 \mathrm{Tr}(\mathbf{E}(x) \cdot \mathbf{B}(x)), \\ \Theta_{ij}(x) &= 2 g^2 \mathrm{Tr}(\theta^B_{ij}(x) - \theta^E_{ij}(x)), \end{aligned} \tag{3}$$

where θ^E and θ^B are the traceless, symmetric chromoelectric and magnetic tensors,

$$\theta^E_{ij} = \mathrm{Tr} E_i E_j - \tfrac{1}{3} \delta_{ij} \mathrm{Tr} \mathbf{E}^2, \qquad \theta^B_{ij} = \mathrm{Tr} B_i B_j - \tfrac{1}{3} \delta_{ij} \mathrm{Tr} \mathbf{B}^2. \tag{4}$$

The scalar operators $\mathrm{Tr}\mathbf{B}^2(x)$ and $\mathrm{Tr}\mathbf{E}^2(x)$, the pseudoscalar $\mathrm{Tr}\mathbf{E}(x) \cdot \mathbf{B}(x)$, and the tensors θ^E, θ^B, are all irreducible representations of the three-dimensional rotation group $SO(3)$.

Denoting the normalized scalar, pseudoscalar, and the tensor glueball states as $|S\rangle$, $|P\rangle$, and $|T_{ij}\rangle$, respectively, the nonzero glueball-to-vacuum matrix elements for their annihilation at rest by these operators are

$$\begin{aligned} (2\pi)^3 \delta^3(\mathbf{0}) f_{(S,B)} &= g^2 \langle 0 | \int d^3x \mathrm{Tr}\mathbf{B}^2(x) | S \rangle, \\ (2\pi)^3 \delta^3(\mathbf{0}) f_{(S,E)} &= g^2 \langle 0 | \int d^3x \mathrm{Tr}\mathbf{E}^2(x) | S \rangle, \\ (2\pi)^3 \delta^3(\mathbf{0}) f_{(T,B)} &= g^2 \langle 0 | \int d^3x \mathrm{Tr}\theta^B_{ij}(x) | T_{ij} \rangle, \\ (2\pi)^3 \delta^3(\mathbf{0}) f_{(T,E)} &= g^2 \langle 0 | \int d^3x \mathrm{Tr}\theta^E_{ij}(x) | T_{ij} \rangle, \\ (2\pi)^3 \delta^3(\mathbf{0}) f_{(PS)} &= g^2 \langle 0 | \int d^3x \mathrm{Tr}\mathbf{E}(x) \cdot \mathbf{B}(x) | P \rangle, \end{aligned} \tag{5}$$

where no implicit summation is applied. It is straightforward to reproduce the matrix elements of the scalar $S(x)$ and pseudoscalar operator $P(x)$ by these quantities, but for the Lorentz tensor $\Theta_{\mu\nu}$, the situation is more complicated. First of all, any hadron state $|h\rangle$ is an eigenstate of $\Theta_{0\mu}$, so that the matrix elements $\langle 0 | \Theta_{0\mu}(x) | h \rangle$ are zero. Together with the traceless property ($\sum_\mu \Theta_{\mu\mu} = 0$), the above condition implies that $\langle 0 | \sum_i \Theta_{ii}(x) | h \rangle$ is zero. Therefore, there are only five linearly independent nonzero matrix elements of $\Theta_{\mu\nu}$, which can be decomposed into the color-magnetic part and the color-electric part,

$$\langle 0 | \Theta_{ij}(x) | T_{ij} \rangle = 2 \langle 0 | \theta^B_{ij}(x) - \theta^E_{ij}(x) | T_{ij} \rangle. \tag{6}$$

Because of the rotational invariance, the five polarizations give the same matrix element of the tensor.

The Lorentz invariance is broken on the spacetime lattice. The zero-momentum stationary glueball state on the lattice must be an irreducible representation (irrep) of the lattice symmetry group, i.e. the 24-element octahedral point group O. The irreps of group O are classified as A_1, A_2, E, T_1, and T_2, which are the counterparts of angular momentum J for the $SO(3)$ rotational group and have dimensions 1, 1, 2, 3, and 3, respectively. Together with parity P and charge conjugate C transformations, the full symmetry group of simple cubic lattice is $O \bigotimes P \bigotimes C$ and the total quantum number of the lattice glueball state is R^{PC}, where R stands for A_1, A_2, E, T_1, or T_2, and PC can be $++$, $+-$, $-+$, or $--$. As mentioned above, we are interested in the matrix elements of the scalar, pseudosca-

lar, and tensor operators, which correspond to the irreps R^{PC} through the following relation: $0^{++} \leftrightarrow A_1^{++}$, $0^{-+} \leftrightarrow A_1^{-+}$, and $2^{++} \leftrightarrow E^{++} \oplus T_2^{++}$. The zero-momentum operators are obtained by summing up all the local operators on the same time-slice in each channel. The dimensionless lattice operators are given below explicitly.

The magnetic and electric scalar (labeled (S, B) and (S, E), respectively) belong to the A_1^{++} representation and are defined as

$$O^{(S,B)}(t) = \frac{g^2 a_s^4}{L^3} \sum_{\mathbf{x}_i} \mathrm{Tr}\mathbf{B}^2(\mathbf{x}_i, t),$$
$$O^{(S,E)}(t) = \frac{g^2 a_s^4}{L^3} \sum_{\mathbf{x}_i} \mathrm{Tr}\mathbf{E}^2(\mathbf{x}_i, t), \tag{7}$$

while the pseudoscalar (labeled (P)) belongs to the A_1^{-+} representation and is defined as

$$O^{(PS)}(t) = \frac{g^2 a_s^4}{L^3} \sum_{\mathbf{x}_i} \mathrm{Tr}\mathbf{E}(\mathbf{x}_i, t) \cdot \mathbf{B}(\mathbf{x}_i, t). \tag{8}$$

In the above questions, L^3 is the dimensionless spatial volume of the lattice and a_s the spatial lattice spacing. For the spin-two irrep of $SO(3)$, the five polarizations are split across the E and T_2 irreps of O and so the tensor operators must be decomposed into their E and T_2 irreducible contents. The four resulting lattice operators are labeled (E, B), (E, E), (T_2, B), and (T_2, E), and are given in terms of their continuum counterparts as

$$O_1^{(T_2,B)}(t) = \frac{g^2 a_s^4}{L^3} \sum_{\mathbf{x}_i} \mathrm{Tr}B_2 B_3(\mathbf{x}_i, t),$$
$$O_2^{(T_2,B)}(t) = \frac{g^2 a_s^4}{L^3} \sum_{\mathbf{x}_i} \mathrm{Tr}B_3 B_1(\mathbf{x}_i, t),$$
$$O_3^{(T_2,B)}(t) = \frac{g^2 a_s^4}{L^3} \sum_{\mathbf{x}_i} \mathrm{Tr}B_1 B_2(\mathbf{x}_i, t),$$
$$O_1^{(T_2,E)}(t) = \frac{g^2 a_s^4}{L^3} \sum_{\mathbf{x}_i} \mathrm{Tr}E_2 E_3(\mathbf{x}_i, t),$$
$$O_2^{(T_2,E)}(t) = \frac{g^2 a_s^4}{L^3} \sum_{\mathbf{x}_i} \mathrm{Tr}E_3 E_1(\mathbf{x}_i, t),$$
$$O_3^{(T_2,E)}(t) = \frac{g^2 a_s^4}{L^3} \sum_{\mathbf{x}_i} \mathrm{Tr}E_1 E_2(\mathbf{x}_i, t), \tag{9}$$

$$O_1^{(E,B)}(t) = \frac{g^2 a_s^4}{L^3} \sum_{\mathbf{x}_i} \frac{1}{2} \mathrm{Tr}[B_1^2 - B_2^2](\mathbf{x}_i, t),$$
$$O_2^{(E,B)}(t) = \frac{g^2 a_s^4}{L^3} \sum_{\mathbf{x}_i} \frac{1}{2\sqrt{3}} \mathrm{Tr}[2B_3^2 - B_1^2 - B_2^2](\mathbf{x}_i, t),$$
$$O_1^{(E,E)}(t) = \frac{g^2 a_s^4}{L^3} \sum_{\mathbf{x}_i} \frac{1}{2} \mathrm{Tr}[E_1^2 - E_2^2](\mathbf{x}_i, t),$$
$$O_2^{(E,E)}(t) = \frac{g^2 a_s^4}{L^3} \sum_{\mathbf{x}_i} \frac{1}{2\sqrt{3}} \mathrm{Tr}[2E_3^2 - E_1^2 - E_2^2](\mathbf{x}_i, t), \tag{10}$$

where the coefficients guarantee that the five components are normalized. Thus we have seven different matrix elements to be calculated on the lattice,

$$T(S, B) = \langle 0|O^{(S,B)}|A_1^{++}\rangle,$$
$$T(S, E) = \langle 0|O^{(S,E)}|A_1^{++}\rangle,$$
$$T(E, B) = \tfrac{1}{2}\langle 0|O_1^{(E,B)} + O_2^{(E,B)}|E^{++}\rangle,$$
$$T(E, E) = \tfrac{1}{2}\langle 0|O_1^{(E,E)} + O_2^{(E,E)}|E^{++}\rangle,$$
$$T(T_2, B) = \tfrac{1}{3}\langle 0|O_1^{(T_2,B)} + O_2^{(T_2,B)} + O_3^{(T_2,B)}|T_2^{++}\rangle,$$
$$T(T_2, E) = \tfrac{1}{3}\langle 0|O_1^{(T_2,E)} + O_2^{(T_2,E)} + O_3^{(T_2,E)}|T_2^{++}\rangle,$$
$$T(PS) = \langle 0|O^{(PS)}|A_1^{-+}\rangle. \tag{11}$$

However, in the practical lattice study, the operators $O^R(t)$ (with R representing the labels mentioned above) are not constructed directly by B_i or E_i, but by the proper combinations of different Wilson loops. The first definition is based on the linear combination of a set of basic Wilson loops with the requirement that the small-a expansion of each combination give the correct continuum form shown, respectively, in Eq. (7)–(11). We call the local operators through this definition Type-I operators. The second construction is that the lattice version of B_i and E_i are defined first by Wilson loops and are used to compose the local operators according to Eq. (7)–(11). The local operators through this construction are denoted Type-II.

The following details the constructions of Type-I and Type-II local operators on the anisotropic lattice with the spatial lattice spacing a_s and the temporal lattice spacing a_t. With the tadpole improvement [8], the tree-level Symanzik's improvement scheme is implemented to reduce the lattice artifact in defining the local operators. Since the aspect ratio of the anisotropic lattice, $\xi = a_s/a_t$, is always set to be much larger than 1, the leading discretization errors in the local operators are at $O(a_t^2, a_s^4, \alpha_s a_s^2)$ in this work.

A. Type-I operator

The Type-I operators are constructed from a set of basic Wilson loops as illustrated in Fig. 1 and Table I, which are chosen by the requirement that the first terms of the small-a expansion of these loops give the desired contin-

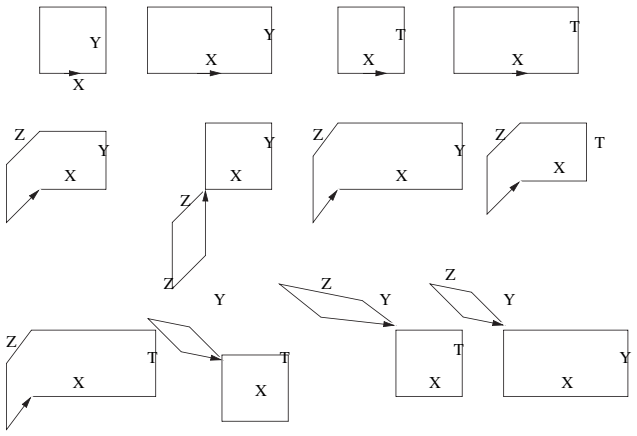

FIG. 1. Wilson loops used in making the Type-I gluonic operators.

TABLE II. The 24 symmetric operations of the cubic point group O are represented by the coordinate transformation.

Index	Operation	Index	Operation
1	$(x, y, z) \rightarrow (x, y, z)$	13	$(x, y, z) \rightarrow (-z, y, x)$
2	$(x, y, z) \rightarrow (-z, -y, -x)$	14	$(x, y, z) \rightarrow (-x, -y, z)$
3	$(x, y, z) \rightarrow (z, x, y)$	15	$(x, y, z) \rightarrow (-y, x, z)$
4	$(x, y, z) \rightarrow (-y, -x, -z)$	16	$(x, y, z) \rightarrow (-z, -x, y)$
5	$(x, y, z) \rightarrow (y, z, x)$	17	$(x, y, z) \rightarrow (-x, z, y)$
6	$(x, y, z) \rightarrow (-x, -z, -y)$	18	$(x, y, z) \rightarrow (-y, -z, x)$
7	$(x, y, z) \rightarrow (z, y, -x)$	19	$(x, y, z) \rightarrow (-x, y, -z)$
8	$(x, y, z) \rightarrow (x, -y, -z)$	20	$(x, y, z) \rightarrow (z, -y, x)$
9	$(x, y, z) \rightarrow (y, x, -z)$	21	$(x, y, z) \rightarrow (-z, x, -y)$
10	$(x, y, z) \rightarrow (z, -x, -y)$	22	$(x, y, z) \rightarrow (y, -x, z)$
11	$(x, y, z) \rightarrow (x, z, -y)$	23	$(x, y, z) \rightarrow (-y, z, -x)$
12	$(x, y, z) \rightarrow (y, -z, -x)$	24	$(x, y, z) \rightarrow (x, -z, y)$

uum operator forms discussed above. We take the following steps in the construction. First, this set of Wilson loops are acted on by the 24 symmetry operations of the cubic point group O (as listed in the Table II), resulting in 24 copies with different orientations for each type of Wilson loops. Next, they are linearly combined to realize the irreps of the group O. The coefficients for each irreps, say, A_1, E, and T_2, are listed in Table III. To reduce the lattice artifact due to the finite lattice spacing, the tree-level Symanzik's improvement is used, which means that differently shaped Wilson loops are combined to construct one operator so that the lattice artifacts are pushed to higher order of lattice spacing. Tadpole improvement is also implemented to improve the reliability of the lattice spacing expansion at the tree level [8].

Apart from the rotational symmetry, the constructed operators should have also definite parity and charge conjugation properties. The symmetric/antisymmetric combination of a Wilson loop and its parity-transformed counterparts gives the positive/negative parity. The $C = +$ operators can be realized by taking the real part of a Wilson loop.

Any operator that includes the chromoelectric field will involve loops with finite extent in the time direction. Operators must be defined for a chosen value of t. The simplest way to enforce this definition is to ensure the operators on time-slice t are eigenstates of the time reversal operators, T about that time slice. The eigenvalue of this reversal must be the same as the parity of the field operator to ensure the correct dimension-four operator is reproduced. The chromoelectric scalar and tensor operators transform positively under T, while the pseudoscalar transforms negatively. The combination coefficients of the time-reversed loops are the products of coefficients of original loops and the time reversal eigenvalues of the time-reversed operator.

TABLE I. The Wilson loops used in the construction of the Type-I gluonic operators. They are illustrated by the ordered paths in the table, where X,Y,Z, and T are directions and the minus sign indicates the path going in the negative direction of that axis. (l_s,l_t) give the numbers of the spatial and temporal links involved in the Wilson loop. These numbers also give the powers of the tadpole parameter.

Index i	Name	Prototype path $C_{i,1}$	No. of Links (l_s,l_t)
1	S-Plaquette	$[X, Y, -X, -Y]$	(4,0)
2	S-Rectangle	$[X, X, Y, -X, -X, -Y]$	(6,0)
3	T-Plaquette	$[X, T, -X, -T]$	(2,2)
4	T-Rectangle	$[X, X, T, -X, -X, -T]$	(4,2)
5	S-Chair	$[X, Y, -X, Z, -Y, -Z]$	(6,0)
6	S-Butterfly	$[X, Y, -X, -Y, Z, -Y, -Z, Y]$	(8,0)
7	S-Sunbed	$[X, X, Y, -X, -X, Z, -Y, -Z]$	(8,0)
8	T-Chair	$[X, T, -X, Z, -T, -Z]$	(4,2)
9	T-Sunbed	$[X, X, T, -X, -X, Z, -T, -Z]$	(6,2)
10	Knot	$[X, T, -X, -T, Z, -Y, -Z, Y]$	(6,2)
11	LS-Knot	$[X, T, -X, -T, Z, Z, -Y, -Z, -Z, Y]$	(8,2)
12	LT-Knot	$[X, X, T, -X, -X, -T, Z, -Y, -Z, Y]$	(8,2)

TABLE III. Combinational coefficients used in Eq. (12) to construct the irreps of the cubic point group.

$r \in O$	$\alpha_r^{A_1}$	$\alpha_r^{E^+}(1,1)$	$\alpha_r^{E^+}(1,2)$	$\alpha_r^{E^+}(2,1)$	$\alpha_r^{E^+}(2,2)$	$\alpha_r^{T_2^+}(2,1)$	$\alpha_r^{T_2^+}(2,2)$	$\alpha_r^{T_2^+}(2,3)$
1	1	-1	$-\frac{1}{\sqrt{3}}$	$-\frac{1}{\sqrt{3}}$	1	0	1	0
2	1	-1	$-\frac{1}{\sqrt{3}}$	$\frac{1}{\sqrt{3}}$	-1	0	1	0
3	1	1	$-\frac{1}{\sqrt{3}}$	$-\frac{1}{\sqrt{3}}$	-1	0	0	1
4	1	1	$-\frac{1}{\sqrt{3}}$	$\frac{1}{\sqrt{3}}$	1	0	0	1
5	1	0	$\frac{2}{\sqrt{3}}$	$\frac{2}{\sqrt{3}}$	0	1	0	0
6	1	0	$\frac{2}{\sqrt{3}}$	$\frac{2}{\sqrt{3}}$	0	1	0	0
7	1	-1	$-\frac{1}{\sqrt{3}}$	$\frac{1}{\sqrt{3}}$	-1	0	-1	0
8	1	-1	$-\frac{1}{\sqrt{3}}$	$-\frac{1}{\sqrt{3}}$	1	0	-1	0
9	1	1	$-\frac{1}{\sqrt{3}}$	$\frac{1}{\sqrt{3}}$	1	0	0	-1
10	1	1	$-\frac{1}{\sqrt{3}}$	$-\frac{1}{\sqrt{3}}$	-1	0	0	-1
11	1	0	$\frac{2}{\sqrt{3}}$	$-\frac{2}{\sqrt{3}}$	0	-1	0	0
12	1	0	$\frac{2}{\sqrt{3}}$	$\frac{2}{\sqrt{3}}$	0	-1	0	0
13	1	-1	$-\frac{1}{\sqrt{3}}$	$\frac{1}{\sqrt{3}}$	-1	0	-1	0
14	1	-1	$-\frac{1}{\sqrt{3}}$	$-\frac{1}{\sqrt{3}}$	1	0	-1	0
15	1	1	$-\frac{1}{\sqrt{3}}$	$\frac{1}{\sqrt{3}}$	1	0	0	-1
16	1	1	$-\frac{1}{\sqrt{3}}$	$-\frac{1}{\sqrt{3}}$	-1	0	0	-1
17	1	0	$\frac{2}{\sqrt{3}}$	$-\frac{2}{\sqrt{3}}$	0	-1	0	0
18	1	0	$\frac{2}{\sqrt{3}}$	$\frac{2}{\sqrt{3}}$	0	-1	0	0
19	1	-1	$-\frac{1}{\sqrt{3}}$	$-\frac{1}{\sqrt{3}}$	1	0	1	0
20	1	-1	$-\frac{1}{\sqrt{3}}$	$\frac{1}{\sqrt{3}}$	-1	0	1	0
21	1	1	$-\frac{1}{\sqrt{3}}$	$-\frac{1}{\sqrt{3}}$	-1	0	0	1
22	1	1	$-\frac{1}{\sqrt{3}}$	$\frac{1}{\sqrt{3}}$	1	0	0	1
23	1	0	$\frac{2}{\sqrt{3}}$	$\frac{2}{\sqrt{3}}$	0	1	0	0
24	1	0	$\frac{2}{\sqrt{3}}$	$-\frac{2}{\sqrt{3}}$	0	1	0	0

It should be noted that the combination coefficients are independent of the shape of loops and each irreducible representation corresponds to a specific set of combination coefficients, denoted by $\alpha_r^{(R)}$, $r = 1, 2, \ldots, 24$.

For clarity, we give the explicit formula of the 13 zero-momentum gluonic operators as follows:

$$
\begin{aligned}
O^{(S,B)}(t) &= \sum_{r,x}\left(\frac{5}{12u_s^4}\mathrm{ReTr}[1 - U_{C_{1,r}}(x,t)] - \frac{1}{24u_s^6}\mathrm{ReTr}[1 - U_{C_{2,r}}(x,t)]\right),\\
O^{(S,E)}(t) &= \xi^2\sum_{r,x}\left(\frac{1}{12u_s^2u_t^2}\mathrm{ReTr}[1 - U_{C_{3,r}}(x,t)] - \frac{1}{192u_s^4u_t^2}\mathrm{ReTr}[1 - U_{C_{4,r}}(x,t)]\right),\\
O_i^{(T_E,B)}(t) &= \sum_{r,x}\left\{\alpha_r^{E^+}(1,i)\left(\frac{5}{12u_s^4}\mathrm{ReTr}U_{C_{1,r}}(x,t) - \frac{1}{96u_s^6}\mathrm{ReTr}U_{C_{2,r}}(x,t)\right) + \alpha_r^{E^+}(2,i)\frac{\sqrt{3}}{96u_s^6}\mathrm{ReTr}U_{C_{2,r}}(x,t)\right\},\\
O_i^{(T_E,E)}(t) &= \xi^2\sum_{r,x}\alpha_r^{E^+}(1,i)\left(\frac{1}{6u_s^2u_t^2}\mathrm{ReTr}U_{C_{3,r}}(x,t) - \frac{1}{96u_s^4u_t^2}\mathrm{ReTr}U_{C_{4,r}}(x,t)\right),\\
O_i^{(T_{T_2},B)}(t) &= \sum_{r,x}\alpha_r^{T_2^+}(2,i)\left(-\frac{11}{96u_s^6}\mathrm{ReTr}U_{C_{5,r}}(x,t) + \frac{1}{96u_s^8}\mathrm{ReTr}U_{C_{6,r}}(x,t) + \frac{1}{48u_s^8}\mathrm{ReTr}U_{C_{7,r}}(x,t)\right),\\
O_i^{(T_{T_2},E)}(t) &= \xi^2\sum_{r,x}\alpha_r^{T_2^+}(2,i)\left(\frac{5}{96u_s^4u_t^2}\mathrm{ReTr}U_{C_{8,r}}(x,t) - \frac{1}{96u_s^6u_t^2}\mathrm{ReTr}U_{C_{9,r}}(x,t)\right),\\
O^{(PS)}(t) &= \xi\sum_{r,x}\alpha_r^{A_1^-}\left(\frac{6}{96u_s^6u_t^2}\mathrm{ReTr}U_{C_{10,r}}(x,t) - \frac{1}{96u_s^8u_t^2}\mathrm{ReTr}U_{C_{11,r}}(x,t) - \frac{1}{192u_s^8u_t^2}\mathrm{ReTr}U_{C_{12,r}}(x,t)\right),
\end{aligned}
\tag{12}
$$

where $U_{C_{i,r}}(x,t)$ is the loop generated by operating rth rotation on the ith prototype loop in Table I. The tadpole parameters u_s and u_t here come from the renormalization of spatial and temporal gauge links, respectively: $U_j(x) \to U_j(x)/u_s$ and $U_t(x) \to U_t(x)/u_t$. The determination of u_s and u_t is described in Section III.

B. Type-II operators

Generally speaking, there can be many ways to define the lattice local operators as long as these definitions give the same continuum limit, and some may have smaller lattice artifacts at finite lattice spacing compared to others. This motivates us to design another type of lattice gluonic operators, called Type-II operators in this work, apart from the construction described above. Both types of operators are used for a self-consistent check.

According to the non-Abelian Stokes theorem [9], a rectangle Wilson loop $P^{a\times b}_{\mu\nu}(x)$ of size $a \times b$, with a, b small, can be expanded as

$$\begin{aligned} P^{a\times b}_{\mu\nu}(x) = \mathbf{1} &+ ab(F_{\mu\nu}(x) + \tfrac{1}{2}(aD_\mu + bD_\nu)F_{\mu\nu}(x) \\ &+ \tfrac{1}{12}(2a^2D^2_\mu + 3abD_\mu D_\nu + 2b^2D^2_\nu)F_{\mu\nu}(x) \\ &+ \tfrac{1}{24}(a^3D^3_\mu + 2a^2bD^2_\mu D_\nu + 2ab^2D_\mu D^2_\nu \\ &+ b^3D^3_\nu)F_{\mu\nu}(x)) + (ab)^2(\tfrac{1}{2}F^2_{\mu\nu}(x) + \tfrac{1}{2}F_{\mu\nu}(x) \\ &\times (aD_\mu + bD_\nu)F_{\mu\nu}(x) + \tfrac{1}{24}F_{\mu\nu}(x)(a^2D^2_\mu \\ &+ b^2D^2_\nu)F_{\mu\nu}(x)) + \tfrac{1}{6}(ab)^3F^3_{\mu\nu} + O((ab)^4). \end{aligned} \tag{13}$$

For simplicity, the factor ig is absorbed into the quantity $F_{\mu\nu}$ and will be reconsidered when comparing with the continuum form. This expression can be simplified by the clover-type combination which is defined as

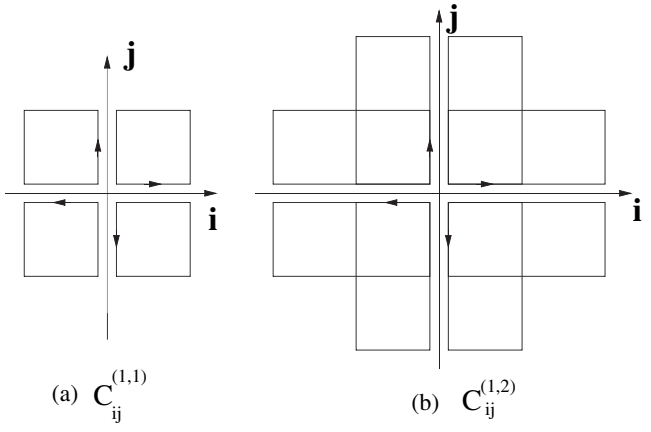

FIG. 2. The clover-shape combinations of spatial plaquette and rectangle, which are used to derive the gauge field strength $F_{\mu\nu}$ on the lattice. Here i and j are the indices of the spatial direction.

$$\begin{aligned} C^{(a,b)}_{\mu\nu}(x) = \tfrac{1}{8}[&(P^{a\times b}_{\mu\nu}(x) + P^{a\times b}_{\nu-\mu}(x) + P^{a\times b}_{-\mu-\nu}(x) \\ &+ P^{a\times b}_{-\nu\mu}(x)) + (P^{b\times a}_{\mu\nu}(x) + P^{b\times a}_{\nu-\mu}(x) \\ &+ P^{b\times a}_{-\mu-\nu}(x) + P^{b\times a}_{-\nu\mu}(x))], \end{aligned} \tag{14}$$

where

$$P_{\pm\mu\pm\nu}(x) = U_{\pm\mu}(x)U_{\pm\nu}(x \pm a\mu)U^\dagger_{\pm\mu}(x \pm b\nu)U^\dagger_{\pm\nu}(x). \tag{15}$$

The small ab expansion of $P_{\pm\mu\pm\nu}(x)$ is similar to Eq. (13) by replacing a and b with $\pm a$ and $\pm b$, respectively. This clover-type combination is illustrated in Fig. 2.

As a result, the tree-level expansion of $C_{\mu\nu}(x)$ is explicitly derived as

$$\begin{aligned} \mathrm{Re}C_{\mu\nu}(x) &= \mathbf{1} + \tfrac{1}{2}(ab)^2F^2_{\mu\nu}(x) + \tfrac{1}{48}(ab)^2(a^2 + b^2) \\ &\quad \times F_{\mu\nu}(x)(D^2_\mu + D^2_\nu)F_{\mu\nu} + O((ab)^4), \\ \mathrm{Im}C_{\mu\nu}(x) &= abF_{\mu\nu}(x) + \tfrac{1}{12}ab(a^2 + b^2)(D^2_\mu + D^2_\nu) \\ &\quad \times F_{\mu\nu}(x) + \tfrac{1}{6}(ab)^3(F_{\mu\nu})^3 + \ldots. \end{aligned} \tag{16}$$

Using $\mathrm{Im}C_{\mu\nu}(x)$ with different a and b as the elementary components, the local operators $F_{\mu\nu}F_{\rho\sigma}$ can be defined through the lattice version of the gauge field strength tensor

$$\begin{aligned} \hat{F}_{\mu\nu}(x) &= \tfrac{1}{3}(5\mathrm{Im}C^{1,1}_{\mu\nu}(x) - \mathrm{Im}C^{1,2}_{\mu\nu}(x)) \\ &= a^2(F_{\mu\nu}(x) - \tfrac{1}{6}a^4(F_{\mu\nu}(x))^3 + O(a^6)), \end{aligned} \tag{17}$$

which is improved up to $O(a^4)$ by the combination of the clover-leaf diagram in Fig. 2(a) and the windmill diagram in Fig. 2(b). Thus the fourth-dimensional gauge operator $F_{\mu\nu}F_{\rho\sigma}$ can be derived from $\hat{F}_{\mu\nu}(x)\hat{F}_{\rho\sigma}(x)$,

$$\begin{aligned} \hat{F}_{\mu\nu}(x)\hat{F}_{\rho\sigma}(x) = a^4F_{\mu\nu}(x)F_{\rho\sigma}(x) &- \tfrac{1}{6}a^8F_{\mu\nu}(F^2_{\mu\nu}(x) \\ &+ F^2_{\rho\sigma}(x))F_{\rho\sigma}(x) + \ldots. \end{aligned} \tag{18}$$

In order to check the effectiveness of the improvement scheme of lattice local operators, we have also derived another lattice definition of $F_{\mu\nu}F_{\rho\sigma}(x)$, which is through the direct combination of $\mathrm{Im}C_{\mu\nu}(x)$, say,

$$\begin{aligned} \widehat{F_{\mu\nu}(x)F_{\rho\sigma}}(x) &= \tfrac{1}{3}(7\mathrm{Im}C^{1,1}_{\mu\nu}(x) \cdot \mathrm{Im}C^{1,1}_{\rho\sigma}(x) - \mathrm{Im}C^{1,1}_{\mu\nu}(x) \\ &\quad \cdot \mathrm{Im}C^{1,2}_{\rho\sigma}(x) - \mathrm{Im}C^{1,2}_{\mu\nu}(x) \cdot \mathrm{Im}C^{1,1}_{\rho\sigma}(x)) \\ &= a^4F_{\mu}\nu(x)F_{\rho\sigma}(x) - \tfrac{1}{6}a^8F_{\mu\nu}(F^2_{\mu\nu}(x) \\ &\quad + F^2_{\rho\sigma}(x))F_{\rho\sigma}(x) - \tfrac{1}{36}a^8(D^2_\mu + D^2_\nu) \\ &\quad \times F_{\mu\nu}(D^2_\rho + D^2_\sigma)F_{\rho\sigma} + \ldots \end{aligned} \tag{19}$$

One can find that, at tree level, the lowest order difference between these two definitions, denoted by Δ, is

$$\Delta = -\tfrac{1}{36}a^8(D^2_\mu + D^2_\nu)F_{\mu\nu}(D^2_\rho + D^2_\sigma)F_{\rho\sigma} + \ldots. \tag{20}$$

In the practical calculation, based on these two approaches, we construct two versions of operators in T^{++}_2 irreps. In Sec. IV, we find the different definitions result in

about 3%–4% discrepancy for the measured matrix elements.

The discussion above is based on the classical (or tree-level) series expansion of Wilson loops. For this to be reliable, the tadpole improvement should be applied, which means the tadpole parameter should be included in the above expressions. Specifically, a n-link spatial Wilson loop $C_{\mu\nu}(x)$ should be divided by a tadpole factor $1/u_s^n$. From the data analysis to be shown in Sec. III that the tadpole improvement alleviates most of the dependence on finite lattice spacing. The improvement scheme of the local operators corresponding to E_iE_j is a little different from that of B_iB_j. Since $a_t \ll a_s$, all the temporal Wilson loops included in the improvement have only one lattice spacing extension in the time direction. In other words, for the temporal loops, we do not include the windmill diagrams which involve two lattice spacing in the time direction. Thus the combination coefficients in the above expression are modified accordingly. We omit the explicit expression here.

III. NUMERICAL DETAILS

Since the implementation of the tadpole improved gauge action on anisotropic lattices was verified to be very successful and efficient in the determination of the glueball spectrum [4], we use the same techniques to calculate the glueball matrix elements. We adopt the anisotropic gauge action used by Morningstar and Peardon in [4]

$$S = \beta\left\{\frac{5}{3}\frac{\Omega_{sp}}{\xi u_s^4} + \frac{4}{3}\frac{\xi\Omega_{tp}}{u_s^2u_t^2} - \frac{1}{12}\frac{\Omega_{sr}}{\xi u_s^6} - \frac{1}{12}\frac{\xi\Omega_{str}}{u_s^4u_t^2}\right\}, \quad (21)$$

where $\beta = 6/g^2$, g is the QCD coupling constant, ξ is the aspect ratio for anisotropy, u_s and u_t are the tadpole-improvement parameters of spatial and temporal gauge links, respectively, and Ω_C's are the sums of various Wilson loops over the total lattice (the explicit expression can be found in Ref. [4]). In practice, u_s is defined by the expectation value of the spatial plaquette, namely, $u_s = (\langle 1/3TrP_{ss'}\rangle)^{1/4}$, and u_t is set to 1. Theoretically, the bare anisotropy ξ should be finely tuned to give the correct physical anisotropy $\xi_{\rm phys} = a_s/a_t$, but in our practical case ξ is always taken as the same as $\xi_{\rm phys}$ because the discrepancy is shown to be within 1–2 percents when the improved action in Eq. (21) is used [4]. For each coupling constant β and ξ, u_s is determined self-consistently in the Monte Carlo updating.

The gauge configurations were generated by using Cabibbo-Marinari (CM) pseudoheatbath and the $SU(2)$ subgroup microcanonical over-relaxation (OR) methods. Three compound sweeps were performed between measurements, where a compound sweep is made up of one CM updating sweep followed by 5 OR sweeps. The measurements of n_{mb} configurations are averaged in each bin, and $n_{\rm bin}$ bins are obtained. Table IV lists the relevant input parameters for lattices with 5 different β. For the case of $\beta = 2.4$, there are three lattice volumes to study the finite-volume effects. In order to calculate the matrix element such as $\langle 0|O|G\rangle$, it is desirable to have the glueball state $|G\rangle$ determined as precisely as possible. In this work, the glueball states $|G\rangle$ with quantum number $R = A_1^{PC}$, A_2^{PC}, E^{PC}, T_1^{PC}, and T_2^{PC} are generated by smeared gluonic operators O_S^R, which are constructed by exploiting link-smearing and variational techniques in a sequence of three steps outlined below. First, for each generated gauge configuration, we perform six smearing/fuzzing schemes to the spatial links, which are various combinations of the single-link procedure (smearing) and the double-link procedure (fuzzing),

TABLE IV. The input parameters for the calculation. Values for the coupling β, anisotropy ξ, the tadpole parameter u_s^4, the single-link smearing parameter λ_s, the double-link smearing parameter λ_f, lattice size, and the number of measurements are listed.

β	ξ	u_s^4	λ_s	λ_f	$L^3 \times T$	$N_{\rm conf}(n_{\rm bins} \times n_{mb})$
2.4	5	0.409	0.1	0.5	$8^3 \times 40$	999×100
					$12^3 \times 64$	100×100
					$16^3 \times 80$	100×100
2.6	5	0.438	0.1	0.5	$12^3 \times 64$	86×100
2.7	5	0.451	0.1	0.5	$12^3 \times 64$	100×100
3.0	3	0.500	0.4	0.5	$16^3 \times 48$	100×100
3.2	3	0.521	0.4	0.5	$24^3 \times 72$	79×100

$$U_j^s(x) = P_{SU(3)}\{U_j(x) + \lambda_s \sum_{\pm(k\neq j)} U_k(x)U_j(x+\hat{k})U_k^\dagger(x+\hat{j})\},$$

$$U_j^f(x) = P_{SU(3)}\{U_j(x)U_j(x+\hat{j}) + \lambda_f \sum_{\pm(k\neq j)} U_k(x)U_j(x+\hat{k}) \times U_j(x+\hat{j}+\hat{k})U_k^\dagger(x+2\hat{j})\}, \quad (22)$$

where $U_j^s(x)$ and $U_j^f(x)$ represent the smearing procedure and the fuzzing procedure, respectively, and $P_{SU(3)}$ denotes the $SU(3)$ projection which is realized through Jacobi method [6] in this work. The six schemes are given explicitly as $s_{\lambda_s}^2$, $s_{\lambda_s}^4$, $s_{\lambda_s}^6$, $f_{\lambda_f} \bigotimes s_{\lambda_s}^2$, $f_{\lambda_f} \bigotimes s_{\lambda_s}^4$, $f_{\lambda_f} \bigotimes s_{\lambda_s}^6$, where s/f denotes smearing/fuzzing procedure defined in Eq. (22). λ_s and λ_f are tunable parameters for smearing and fuzzing and take the optimal value $\lambda_s = 0.1$ (0.4 at $\xi = 3$) and $\lambda_f = 0.5$. Secondly, for each smearing/fuzzing scheme, we use ten Wilson loops illustrated in Fig. 3, which are the same as used in [4], as prototypes to construct the operator $\phi_\alpha^{(R)}(t)$ which is a linear combination of different oriented spatial loops, invariant under spatial transformation, and transforms according to the irreps R. There are four independent constructions for each R (except for A_2^{-+}) for each smearing/fuzzing scheme, thus the operator $O_S^{(R)}(t)$ is a linear combination of 24 operators, $O_S^{(R)} = \sum_\alpha v_\alpha^{(R)}\phi_\alpha^{(R)}(t)$. The coefficients $v_\alpha^{(R)}$ are deter-

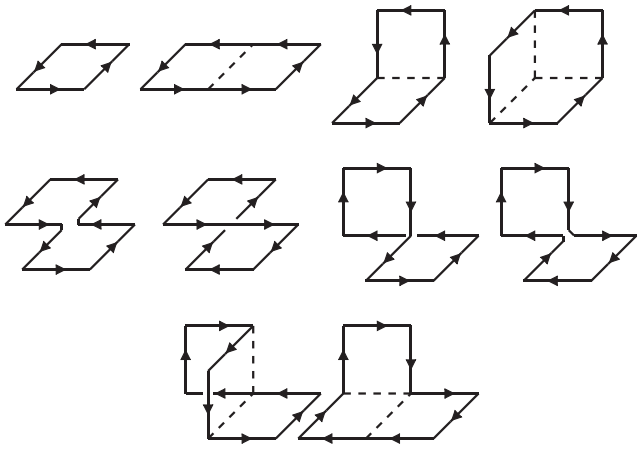

FIG. 3. Wilson loops used in making the smeared glueball operators.

mined by a variational method so that $O_S^{(R)}$ projects mostly to specific glueball states $|G\rangle$.

What we obtain from the MC simulation are the 24×24 correlation matrix

$$\tilde{C}_{\alpha\beta}(t) = \sum_{\tau} \langle 0|\bar{\phi}_{\alpha}^{(R)}(t+\tau)\bar{\phi}_{\beta}^{(R)}(\tau)|0\rangle, \tag{23}$$

where the vacuum subtraction

$$\bar{\phi}_{\alpha}^{(R)}(t) = \phi_{\alpha}^{(R)}(t) - \langle 0|\phi_{\alpha}^{(R)}(t)|0\rangle \tag{24}$$

is only applied to the A_1^{++} channel which has a vacuum expectation value. The coefficients are determined in the data analysis stage by minimizing the effective mass

$$\tilde{m}(t_D) = -\frac{1}{t_D} \ln \frac{\sum_{\alpha\beta} v_{\alpha}^{(R)} v_{\beta}^{(R)} \tilde{C}_{\alpha\beta}(t_D)}{\sum_{\alpha\beta} v_{\alpha}^{(R)} v_{\beta}^{(R)} \tilde{C}_{\alpha\beta}(0)}, \tag{25}$$

where the time separation for optimization is fixed to $t_D = 1$. This is equivalent to solving the generalized eigenvalue equation

$$\tilde{C}(t_D)\mathbf{v}^{(R)} = e^{-t_D \tilde{m}(t_D)} \tilde{C}(0)\mathbf{v}^{(R)} \tag{26}$$

and the eigenvector $\mathbf{v}_0^{(R)}$, corresponding to the lowest effective mass $\tilde{m}_0(t_D)$, yields the coefficients $v_{0\alpha}^{(R)}$ for the operator $O_S^{(R)}(t)$ which, under ordinary circumstances, best overlaps with the lowest-lying glueball G_0 in the channel of interest. The operators most overlapping with the excited states can also be constructed accordingly.

After the smeared operators are determined, the glueball masses and the matrix elements we are concerned with can be extracted by fitting two two-point functions, namely, the smeared-smeared correlation function,

$$\begin{aligned} C_{SS}(t) &= \sum_{\tau} \langle 0|O_S(t+\tau)O_S(\tau)|0\rangle \\ &= \sum_{n} \frac{1}{2M_n V} \langle 0|O_S|n\rangle\langle n|O_S|0\rangle e^{-m_n t} \\ &\sim \frac{1}{2m_G V} |\langle G|O_S|0\rangle|^2 e^{-M_G t} (t \to \infty), \end{aligned} \tag{27}$$

and the smeared-local one

$$\begin{aligned} C_{SL}(t) &= \sum_{\tau} \langle 0|O_S(t+\tau)O_L(\tau)|0\rangle \\ &= \sum_{n} \frac{1}{2M_n V} \langle 0|O_S|n\rangle\langle n|O_L|0\rangle e^{-m_n t} \\ &\sim \frac{1}{2M_G V} \langle G|O_S|0\rangle\langle 0|O_L|G\rangle e^{-M_G t} (t \to \infty). \end{aligned} \tag{28}$$

$C_{SS}(t)$ and $C_{SL}(t)$ can be fitted simultaneously with three parameters, i.e., $\langle 0|O_S|G\rangle$, $\langle 0|O_L|G\rangle$, and the ground state glueball mass M_G. $\langle 0|O_L|G\rangle$ is the glueball matrix element we would like to obtain. Of course, before the physical results can be derived, a proper renormalization scheme should be performed.

In the following, we describe the calculation details step by step.

A. Setting the scale using the static potential

The five lattice spacings a_s are determined by calculating the heavy quark static potential. This part of the calculation is independent of the production runs. The static-quark potential $V(\mathbf{r})$ can be extracted from the averages of Wilson loops $W(\mathbf{r}, t)$,

$$W(\mathbf{r}, t) = Z(\mathbf{r}) \exp(-tV(\mathbf{r})) + \ldots \tag{29}$$

which can be measured precisely on the lattice. For each β, 200 configurations are generated, each of which is separated by 30 compound sweeps so that the autocorrelation effects are reduced. Secondly, these configurations are fixed to temporal gauge so that the Wilson loops can be calculated more easily. Different smearing schemes are applied to Wilson loops with different size to increase the overlapping with the ground states. Finally, the static potential is fitted by the model

$$V(\mathbf{r}) = V_0 + \sigma r + \frac{e_c}{r}, \tag{30}$$

with three parameters V_0, σ, and e_c in the correlated fit method. The lattice spacing a_s is determined by

$$\frac{a_s}{r_0} = \sqrt{\frac{\sigma a_s^2}{1.65 + e_c}}, \tag{31}$$

according to the relation $r^2 dV(\mathbf{r})/dr]_{r=r_0} = 1.65$, where r_0 is hadronic scale parameter [10]. The lattice spacings for different β are listed in Table V.

TABLE V. The lattice spacings determined by $r_0^{-1} = 410(20)$ MeV at different β.

β	r_0/a_s	a_s/r_0	a_s (fm)
2.4	2.17(1)	0.461(2)	0.222(1)
2.6	2.74(2)	0.365(2)	0.176(1)
2.7	3.09(2)	0.326(2)	0.156(1)
3.0	4.05(4)	0.247(2)	0.119(1)
3.2	4.76(5)	0.210(2)	0.101(1)

B. The glueball mass spectrum

Glueball masses can be obtained by fitting the two-point functions $C_{SS}(t)$ directly. It is taken as a testimony of the effectiveness of the improvement and smearing scheme [4]. Even though we are interested in the glueball matrix elements of the four channels A_1^{++}, A_1^{-+}, E^{++}, and T_2^{++} in this work, glueball masses of all the 20 channels R^{PC} are calculated as a by-product.

After the implementation of variational optimization in each channel, we can obtain a specific operator which overlaps most with the specific state and has little contaminations from other states with the same J^{PC}, so that we can use a single mass term

$$C_{SS}(t) = Z(e^{-Mt} + e^{-M(T-t)}), \tag{32}$$

to fit the two-point function in a time range $t_{\min}, \ldots, t_{\max}$, which can be determined by observing the effective mass plateau. As a convention in this work, we use M_G to represent the mass of a glueball state in the physical units and M to represent the dimensionless mass parameter in the data processing with the relation $M = M_G a_t$. Generally speaking, for most channels in each of the five β cases, the overlap of the specific operators on the ground states are all larger than 90%.

Before performing the continuum extrapolation, we check the finite-volume effects of glueball masses. Three independent calculations at $\beta = 2.4$, $\xi = 5$ were carried out on a $8^3 \times 40$ lattice, a $12^3 \times 64$, and a $16^3 \times 80$ lattice. These lattices have spatial volumes of $(1.76\ \text{fm})^3$, $(2.64\ \text{fm})^3$, and $(3.52\ \text{fm})^3$, respectively, with the lattice spacing $a_s \sim 0.22$ fm from $r_0^{-1} = 410(20)$ MeV. For these three runs, all the input parameters are the same except the different lattice volume.

The calculated glueball mass spectra are listed in Table VI, where one can find at a glance that the finite-volume effects are very small and in most cases the changes are within errors and consistent with zero statistically. More precisely, we use the following scheme to illustrate the finite-volume effect (FVE) quantitatively. Let $\bar{M}$ denote the average value of the glueball masses from the three lattice volumes, $M(L)$ denotes the glueball mass measured on lattice $L^3 \times T$. The fractional change of the glueball mass is defined by $\delta_G(L) = 1 - M(L)/\bar{M}$. The results for these fractional changes are shown in Fig. 4. Each point in the figure shows the fractional change

TABLE VI. The fitted ground state masses in the 20 R^{PC} channels at $\beta = 2.4$ and $\xi = 5$ on three different lattices $L^3 \times T = 16^3 \times 80$, $12^3 \times 64$, and $8^3 \times 40$.

	$L = 16$	$L = 12$	$L = 8$
A_1^{++}	0.308(3)	0.308(2)	0.312(2)
A_1^{+-}	1.082(14)	1.051(13)	1.079(10)
A_1^{-+}	0.604(11)	0.618(4)	0.618(3)
A_1^{--}	1.03(3)	1.075(16)	1.01(3)
A_2^{++}	0.825(8)	0.818(8)	0.820(5)
A_2^{+-}	0.805(6)	0.804(8)	0.808(5)
A_2^{-+}	1.047(10)	1.067(12)	1.053(12)
A_2^{--}	0.993(11)	0.976(10)	0.994(27)
E^{++}	0.542(3)	0.536(2)	0.541(2)
E^{+-}	0.919(17)	0.957(8)	0.960(6)
E^{-+}	0.699(4)	0.698(4)	0.695(3)
E^{--}	0.879(5)	0.891(7)	0.882(5)
T_1^{++}	0.826(5)	0.832(4)	0.834(3)
T_1^{+-}	0.657(6)	0.661(5)	0.663(4)
T_1^{-+}	0.932(5)	0.940(5)	0.936(4)
T_1^{--}	0.865(12)	0.884(5)	0.893(4)
T_2^{++}	0.542(3)	0.536(3)	0.538(2)
T_2^{+-}	0.807(4)	0.808(11)	0.799(8)
T_2^{-+}	0.697(5)	0.700(4)	0.700(2)
T_2^{--}	0.903(4)	0.893(6)	0.896(3)

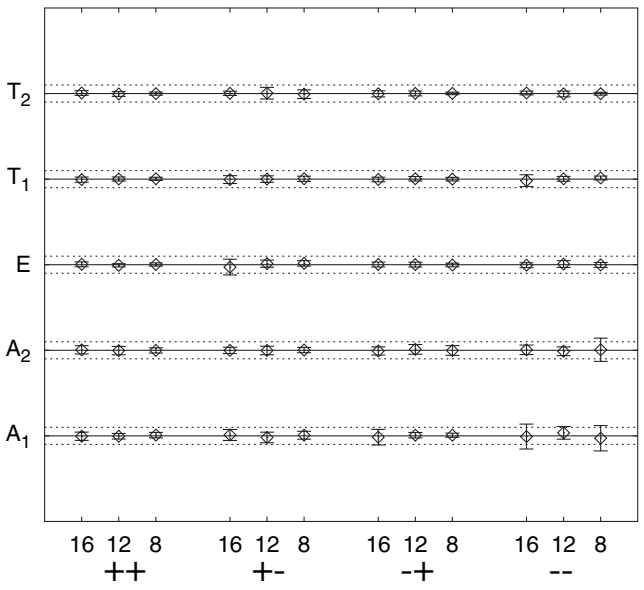

FIG. 4. Finite-volume effects of glueball masses at $\beta = 2.4$, $\xi = 5$. Each point shows the fractional change $\delta_G(L) = 1 - M(L)/\bar{M}$ of the glueball mass, where $M(L)$ is the glueball mass measured on the lattice $L^3 \times T$ with $L = 8$, 12, and 16, and $\bar{M}$ is the average value over those from different lattices. The errorbars come from the statistical errors of $M(L)$. The lattice labels L are shown along the horizontal axis, and the labels along the vertical axis are the irreps of lattice symmetry group. The solid lines indicate $\delta_G = 0$, the dotted lines above the solid lines indicate $\delta_G = 0.02$, and the dotted lines below the solid lines indicate $\delta_G = -0.02$.

$\delta_G(L)$ of the glueball mass, the error bars come from the statistical errors of $M(L)$, the solid lines indicate $\delta_G = 0$, the dotted lines above and below the solid lines indicate $\delta_G = 0.02$ and $\delta_G = -0.02$, respectively. All changes are statistically consistent with zero, suggesting that systematic errors in these results from finite volume are no larger than the statistical errors for these physical volumes. Since the physical volumes of the other β values are not smaller than the $8^3 \times 40$ at $\beta = 2.4$, we shall neglect the FVE for the higher β results.

The fitted glueball masses at different coupling constant β are listed in Table VII, where the statistical errors are also quoted. The dimensionless products of r_0 and the glueball masses M_G are shown as functions of $(a_s/r_0)^2$. To remove discretization errors from our estimates, the results for each level in these figures must be extrapolated to the continuum limit $a_s/r_0 \to 0$. From perturbation theory, the leading discretization errors are expected to be $O(a_t^2, a_s^4, \alpha_s a_s^2)$. As discussed in Ref. [4], the $O(a_t^2, \alpha_s a_s^2)$ errors could be negligible compared to the $O(a_s^4)$ errors for most calculated glueball masses except for A_1^{++} glueball, so the fit model for these glueball masses is chosen to be

$$M_G(a_s) r_0 = M_G(0) r_0 + c_4 \frac{a_s^4}{r_0^4}. \tag{33}$$

The masses versus $(a_s/r_0)^2$, as well as the fitted curves are shown in Fig. 5–8. One can find from the figures that the data obey this function very well. However, for A_1^{++} glue-

TABLE VII. The fitted ground state masses M in the 20 R^{PC} channels at five different β's. The errors quoted here are all statistical errors from correlated minimal-χ^2 method.

R^{PC}	$\beta = 2.4$	$\beta = 2.6$	$\beta = 2.7$	$\beta = 3.0$	$\beta = 3.2$
A_1^{++}	0.312(2)	0.264(2)	0.247(2)	0.325(3)	0.279(5)
A_1^{+-}	1.079(10)	0.851(17)	0.741(11)	0.961(10)	0.822(13)
A_1^{-+}	0.618(3)	0.470(4)	0.410(3)	0.515(6)	0.439(4)
A_1^{--}	1.01(3)	0.897(20)	0.815(5)	1.036(12)	0.879(19)
A_2^{++}	0.820(5)	0.665(4)	0.593(6)	0.779(17)	0.683(17)
A_2^{+-}	0.808(5)	0.644(7)	0.560(5)	0.721(11)	0.616(8)
A_2^{-+}	1.053(12)	0.850(7)	0.745(26)	1.02(4)	0.868(18)
A_2^{--}	0.994(27)	0.748(5)	0.672(9)	0.827(21)	0.721(9)
E^{++}	0.541(2)	0.418(2)	0.374(3)	0.475(5)	0.414(4)
E^{+-}	0.960(6)	0.745(7)	0.663(13)	0.843(13)	0.734(16)
E^{-+}	0.695(3)	0.543(4)	0.486(3)	0.627(3)	0.514(3)
E^{--}	0.882(5)	0.695(6)	0.623(10)	0.797(29)	0.682(13)
T_1^{++}	0.834(3)	0.645(5)	0.561(3)	0.736(8)	0.628(4)
T_1^{+-}	0.663(4)	0.526(6)	0.459(6)	0.596(9)	0.510(5)
T_1^{-+}	0.936(4)	0.737(7)	0.664(9)	0.844(11)	0.714(6)
T_1^{--}	0.893(4)	0.685(5)	0.610(7)	0.776(8)	0.650(9)
T_2^{++}	0.538(2)	0.419(2)	0.375(4)	0.476(8)	0.413(5)
T_2^{+-}	0.799(8)	0.631(4)	0.568(7)	0.720(7)	0.617(4)
T_2^{-+}	0.700(2)	0.540(3)	0.479(4)	0.604(10)	0.510(3)
T_2^{--}	0.896(3)	0.705(5)	0.642(5)	0.805(23)	0.680(10)

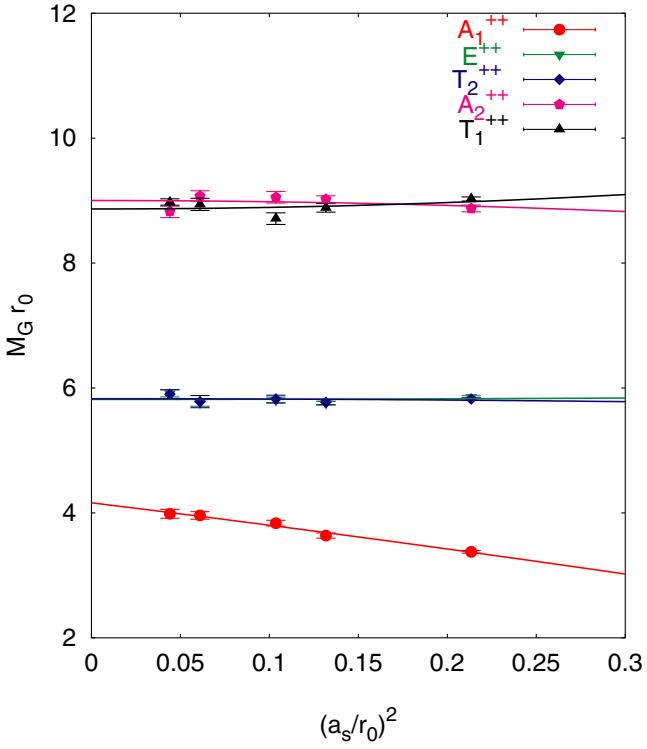

FIG. 5 (color online). Masses of $PC = ++$ glueballs in terms of r_0 against the lattice spacing square $(a_s/r_0)^2$. The calculated values are plotted in points, and the curves are the best fits.

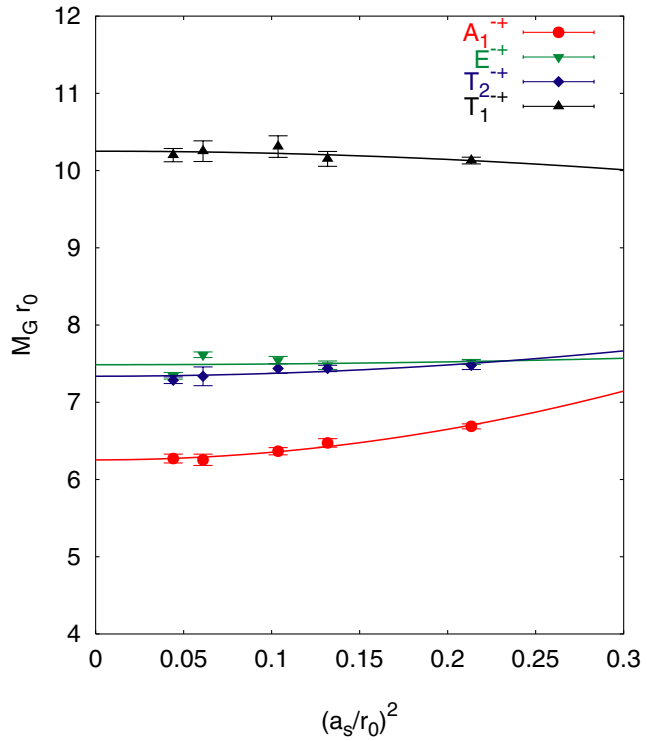

FIG. 6 (color online). Masses of $PC = -+$ glueballs in terms of r_0 against the lattice spacing square $(a_s/r_0)^2$. The calculated values are plotted in points, and the curves are the best fits.

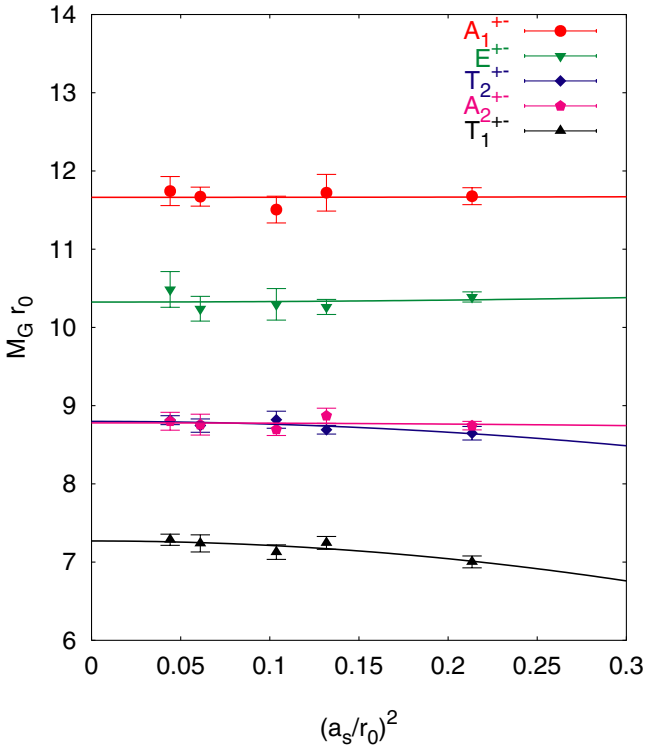

FIG. 7 (color online). Masses of $PC = +-$ glueballs in terms of r_0 against the lattice spacing square $(a_s/r_0)^2$. The calculated values are plotted in points, and the curves are the best fits.

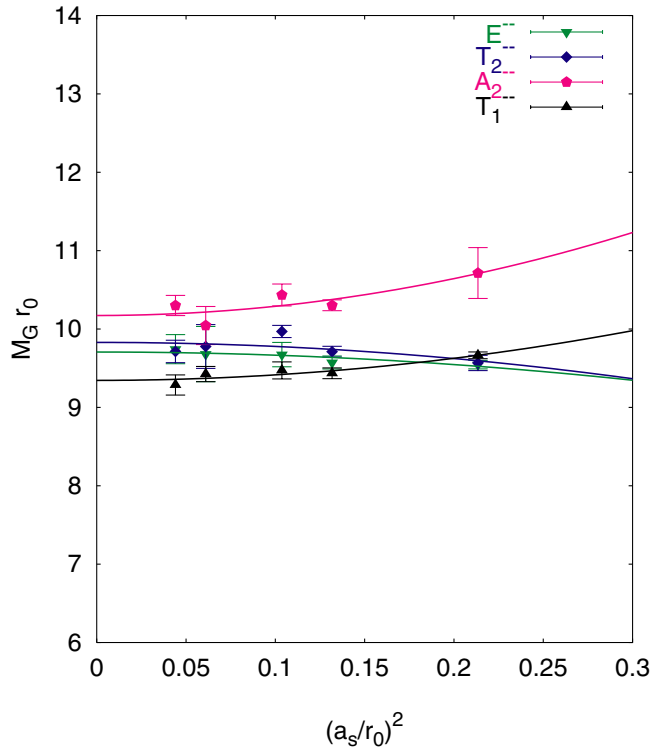

FIG. 8 (color online). Masses of $PC = --$ glueballs in terms of r_0 against the lattice spacing square $(a_s/r_0)^2$. The calculated values are plotted in points, and the curves are the best fits.

TABLE VIII. Continuum-limit glueball masses M_G. The corresponding results in Reference [4] are also quoted for comparison.

R^{PC}	Possible J^{PC}	$r_0 M_G$ (this work)	$r_0 M_G$ [4]
A_1^{++}	0^{++}	4.16(11)	4.21(11)
E^{++}	2^{++}	5.82(5)	5.85(2)
T_2^{++}	2^{++}	5.83(4)	5.85(2)
A_2^{++}	3^{++}	9.00(8)	8.99(4)
T_1^{++}	3^{++}	8.87(8)	8.99(4)
A_1^{-+}	0^{-+}	6.25(6)	6.33(7)
T_1^{+-}	1^{+-}	7.27(4)	7.18(3)
E^{-+}	2^{-+}	7.49(7)	7.55(3)
T_2^{-+}	2^{-+}	7.34(11)	7.55(3)
T_2^{+-}	3^{+-}	8.80(3)	8.66(4)
A_2^{+-}	3^{+-}	8.78(5)	8.66(3)
T_1^{--}	1^{--}	9.34(4)	9.50(4)
E^{--}	2^{--}	9.71(3)	9.59(4)
T_2^{--}	2^{--}	9.83(8)	9.59(4)
A_2^{--}	3^{--}	10.25(4)	10.06(21)
E^{+-}	2^{+-}	10.32(7)	10.10(7)
A_1^{+-}	0^{+-}	11.66(7)	11.57(12)

ball mass, the $O(a_s^2)$ error seems still very large. So we keep the linear term of a_s^2 in the fit model, namely,

$$M_G(a_s) r_0 = M_G(0) r_0 + c_2 \frac{a_s^2}{r_0^2} + c_4 \frac{a_s^4}{r_0^4}. \tag{34}$$

Already there has been some discussion on the possible reason for this large discretization error in scalar channel; one can refer to Ref. [4] for details.

We list several continuum-extrapolated glueball masses in Table VIII. We note that the earlier work [4] was carried out with $\beta = 1.7$, 1.9, 2.2, 2.4, 2.5, and 3.0. In the present work, we concentrate on finer lattice spacings with $\beta = 2.4$, 2.6, 2.7, 3.0, and 3.2. For comparison, we have listed the results from the previous work [4].

C. The glueball matrix elements

As described above, we use the correlated minimal-χ^2 method to fit the smeared-smeared and smeared-local two-point functions, namely, $C_{SS}(t)$ and $C_{SL}(t)$, simultaneously using the fit functions

$$\begin{aligned} C_{SS}(t) &= X^2(e^{-Mt} + e^{-M(T-t)}), \\ C_{SL}(t) &= XY(e^{-Mt} + e^{-M(T-t)}), \end{aligned} \tag{35}$$

where $X = \langle 0|O_S(0)|G\rangle/\sqrt{2M_G V}$ and $Y = \langle 0|O_L(0)|G\rangle/\sqrt{2M_G V}$. Here V is the spatial lattice volume in physical units, say, $V = L^3 a_s^3$, and $M_G = M a_t^{-1}$. As an example, we show the effective mass plot at $\beta = 2.4$ ($L = 8$ lattice) in Figs. 9 and 10, where the smeared-local correlation functions are plotted on the negative-time side of the t axis. In each channel, the effective mass plateau for C_{SS} is flatter than that of C_{SL}. Nevertheless,

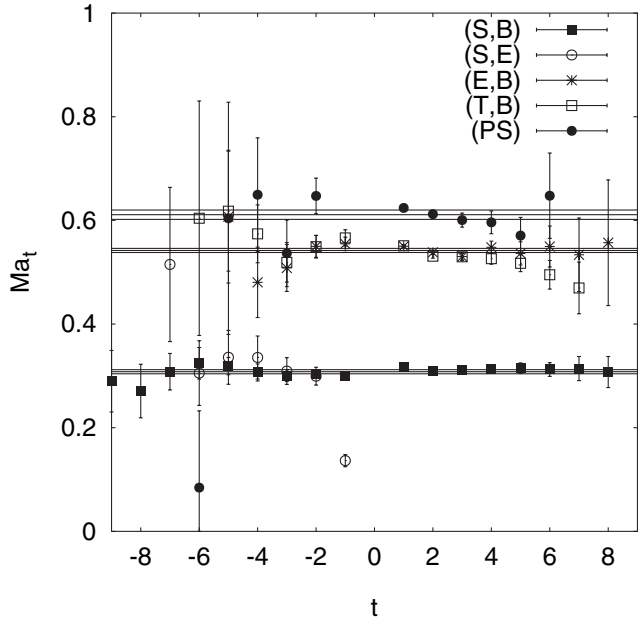

FIG. 9. The effective mass plateaus of the smeared-smeared and smeared-local correlation functions at $\beta = 2.4$, $\xi = 5$ on the lattice $8^3 \times 40$. The smeared-local correlation functions are plotted on the negative-time side of the t axis. The Type-I local operators are used.

both of them can be fitted by the same mass parameter consistently. For all the five β's, the fit parameters X,Y, effective masses M, as well as the fit windows, are listed in Table IX, X, XI, XII, and XIII. In these tables, the first group of data is for Type-I operators, the second group for Type-II operators, and the last two row of data for the second definition (Eq. (19)) of Type-II operators in T_2 irreps. We give a brief interpretation of the meaning of the value of X parameter here. During the practical performance of the variational method discussed in Sec. III, the eigenvectors $\mathbf{v}^{(R)}$ in Eq. (26) are normalized as $\mathbf{v}^{(R)T}\tilde{C}(0)\mathbf{v}^{(R)} = 1$, so that the parameter X indicates the relative overlap of the smeared operator to the specific stationary state (the ground state here). In these tables, all the X parameters are very close to 1 which implies that the smeared operators couple almost completely to the ground state and there is little contamination from excited states. The χ^2's per degree of freedom of the data fitting are all acceptable and also listed in the tables.

From the measured matrix elements of the two definitions of the Type-II local operators in tensor channel (T_2 irreps), we can get an estimate of the $O(a_s^4)$ lattice artifacts. Recalling the discussion in Sec. II, after restoring the fact ig to $F_{\mu\nu}$, the difference of the two definition of the operators (T_2, B) is

$$\Delta = \frac{1}{36} a_s^8 g^2 (D_\mu^2 + D_\nu^2) F_{\mu\nu} (D_\rho^2 + D_\sigma^2) F_{\rho\sigma} + \ldots, \quad (36)$$

with the indices μ, ν, ρ, and σ varying accordingly. The ratio of the matrix elements of the two definitions of operator (T_2, B) is plotted in Fig. 11 with respect to the lattice spacing. It is known that this difference comes totally from

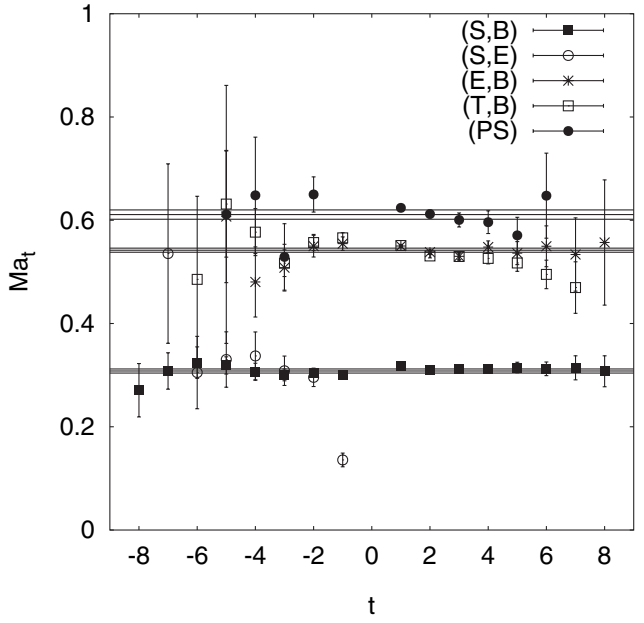

FIG. 10. The effective mass plateaus of the smeared-smeared and smeared-local correlation functions at $\beta = 2.4$, $\xi = 5$ on the lattice $8^3 \times 40$. The smeared-local correlation functions are plotted on the negative-time side of the t axis. The Type-II local operators are used.

TABLE IX. The matrix elements extracted at $\beta = 2.4$ (on lattice $8^3 \times 40$). The smeared-smeared (SS) and smeared-local (SL) correlators are fitted simultaneously in the time window t(SS) and t(SL). The fitted masses M, X, and Y parameters are listed. The first group of data is for Type-I operators, the second group for Type-II operators, and the last two rows of data for the second definition (Eq. (19)) of Type-II operators in T_2 irreps.

R	t(SS)	t(SL)	M	$Y(\times 10^{-2})$	X	χ^2/d.o.f.
(S, B)	1–4	1–3	0.311(2)	21.3(1)	0.994(3)	0.92
(S, E)	1–4	1–4	0.311(2)	21.1(2)	0.994(3)	0.69
(PS)	1–5	2–4	0.617(4)	5.24(11)	0.985(4)	1.59
(E, B)	1–7	1–5	0.541(2)	2.64(3)	0.995(2)	0.64
(E, E)	1–7	1–4	0.541(2)	1.52(9)	0.995(2)	0.64
(T_2, B)	2–7	1–4	0.539(3)	1.84(12)	0.989(2)	0.57
(T_2, E)	2–7	1–3	0.539(3)	0.85(5)	0.990(2)	0.52
(S, B)	1–9	1–7	0.311(2)	11.54(6)	0.993(3)	1.12
(S, E)	1–9	1–7	0.311(2)	16.38(13)	0.995(3)	0.75
(PS)	2–7	1–6	0.617(4)	5.33(11)	0.985(4)	1.36
(E, B)	1–7	1–6	0.541(2)	2.50(2)	0.995(2)	0.89
(E, E)	1–7	1–3	0.542(2)	1.35(4)	0.995(2)	0.87
(T_2, B)	2–7	1–5	0.541(2)	2.24(1)	0.990(3)	1.34
(T_2, E)	2–7	2–4	0.542(2)	0.73(4)	0.989(2)	0.45
(T_2, B)	2–7	2–5	0.543(2)	2.37(1)	0.990(2)	1.06
(T_2, E)	2–7	1–4	0.542(2)	0.73(4)	0.989(2)	0.46

TABLE X. The same as in Table IX, but for $\beta = 2.6$.

R	t(SS)	t(SL)	M	$Y(\times 10^{-2})$	X	χ^2/d.o.f.
(S, B)	1–9	1–7	0.264(2)	6.48(5)	0.994(3)	0.92
(S, E)	1–9	1–7	0.264(2)	6.37(11)	0.994(3)	0.69
(PS)	2–7	1–5	0.470(4)	2.14(3)	0.985(4)	1.59
(E, B)	1–7	1–6	0.424(2)	0.716(10)	0.995(2)	0.64
(E, E)	1–7	1–3	0.423(2)	0.39(4)	0.995(2)	0.64
(T_2, B)	2–7	1–5	0.421(1)	0.562(7)	0.989(2)	0.57
(T_2, E)	2–7	1–4	0.421(2)	0.23(2)	0.990(2)	0.52
(S, B)	1–9	1–7	0.265(2)	4.01(3)	0.993(3)	1.12
(S, E)	1–9	1–7	0.263(2)	5.06(3)	0.995(3)	0.75
(PS)	2–7	1–6	0.470(5)	2.16(3)	0.985(4)	1.36
(E, B)	1–7	1–6	0.424(2)	0.706(13)	0.995(2)	0.89
(E, E)	1–7	1–3	0.424(2)	0.40(3)	0.995(2)	0.87
(T_2, B)	2–7	1–5	0.423(2)	0.698(5)	0.990(3)	1.34
(T_2, E)	2–7	2–4	0.421(2)	0.22(2)	0.989(2)	0.45
(T_2, B)	2–7	2–5	0.422(2)	0.719(10)	0.990(2)	1.06
(T_2, E)	2–7	1–4	0.421(2)	0.22(2)	0.989(2)	0.46

TABLE XII. The same as in Table IX, but for $\beta = 3.0$.

R	t(SS)	t(SL)	M	$Y(\times 10^{-2})$	X	χ^2/d.o.f.
(S, B)	2–9	1–4	0.324(3)	1.56(3)	0.985(3)	0.99
(S, E)	2–9	1–4	0.326(4)	1.50(4)	0.985(3)	0.82
(PS)	2–5	1–4	0.542(6)	0.706(15)	0.981(6)	2.00
(E, B)	3–7	1–4	0.480(6)	0.176(7)	0.967(8)	0.22
(E, E)	3–7	1–3	0.480(6)	0.107(14)	0.967(8)	0.25
(T_2, B)	3–8	1–3	0.487(5)	0.137(5)	0.969(7)	1.28
(T_2, E)	3–8	1–3	0.485(6)	0.060(9)	0.967(7)	0.94
(S, B)	2–9	2–7	0.326(4)	1.07(2)	0.984(3)	0.68
(S, E)	2–9	1–8	0.324(3)	1.09(3)	0.986(3)	0.49
(PS)	2–5	1–4	0.541(6)	0.715(15)	0.981(5)	1.84
(E, B)	3–7	1–4	0.477(6)	0.179(5)	0.964(8)	0.72
(E, E)	3–7	1–3	0.480(6)	0.086(5)	0.967(8)	0.22
(T_2, B)	3–8	1–4	0.490(5)	0.172(4)	0.971(7)	1.55
(T_2, E)	3–8	1–3	0.485(6)	0.053(6)	0.968(8)	1.17
(T_2, B)	3–8	1–4	0.489(5)	0.179(4)	0.971(7)	1.46
(T_2, E)	3–8	1–3	0.485(6)	0.053(6)	0.968(8)	1.17

the lattice discretization and will disappear in the continuum limit. This is the case from the figure. Even though the relative difference is less than 3%–4%, the deviation of the ratio from 1 is detectable on coarse lattice with larger lattice spacing and decreases when approaching to the continuum limit. On the finest lattice we are using, the difference is consistent with zero within the error. This result shows that, as far as the Type-II operators are concerned, after the implementation of Symanzik's improvement scheme along with the tadpole improvement, the measured matrix elements of the two versions of lattice local operator have a few percent differences at finite a_s, but approaches the same continuum limit as a_s goes to zero.

Here comes the discussion of the FVE of the matrix elements. By analogy with the FVE analysis of glueball masses, the glueball matrix elements are also calculated at $\beta = 2.4$ and $\xi = 5$ on a $8^3 \times 40$ lattice, a $12^3 \times 64$, and a $16^3 \times 80$ lattice. For these three runs, all the input parameters are the same except the different lattice volume. The extracted matrix elements are listed in Table XIV, XV, and XVI, respectively, for Type-I and Type-II operators. As illustrated in the tables, the finite-volume effects of matrix elements are very small and in most case the changes are consistent with zero statistically. We also define the relative deviation $\delta_G(L) = 1 - f_G(L)/\bar{f}_G$ to show the FVE quantitatively, where $\bar{f}_G$ is the mean value of the matrix elements of glueball G averaged over the three lattice volumes, $f_G(L)$ denote the matrix element of glueball G

TABLE XI. The same as in Table IX, but for $\beta = 2.7$.

R	t(SS)	t(SL)	M	$Y(\times 10^{-2})$	X	χ^2/d.o.f.
(S, B)	2–9	1–7	0.247(2)	5.03(4)	0.990(3)	0.92
(S, E)	2–9	1–7	0.246(2)	4.88(13)	0.991(3)	0.50
(PS)	1–7	2–6	0.431(3)	1.88(5)	0.991(2)	1.07
(E, B)	3–8	1–4	0.376(3)	0.575(10)	0.982(4)	0.75
(E, E)	3–8	1–3	0.376(4)	0.27(3)	0.981(4)	0.39
(T_2, B)	4–8	2–6	0.379(5)	0.423(10)	0.977(7)	1.14
(T_2, E)	4–8	1–4	0.378(6)	0.20(2)	0.975(8)	1.39
(S, B)	2–9	3–7	0.246(2)	3.21(4)	0.990(3)	0.86
(S, E)	2–9	3–7	0.247(2)	3.80(10)	0.990(3)	0.58
(PS)	2–7	1–6	0.431(2)	1.90(5)	0.991(2)	1.08
(E, B)	3–8	2–5	0.376(3)	0.592(10)	0.981(4)	0.60
(E, E)	3–8	2–5	0.376(3)	0.27(2)	0.982(4)	0.22
(T_2, B)	4–8	2–6	0.386(5)	0.546(10)	0.988(8)	1.79
(T_2, E)	4–8	1–3	0.378(5)	0.19(2)	0.975(8)	1.28
(T_2, B)	4–8	3–6	0.386(5)	0.565(9)	0.987(8)	1.82
(T_2, E)	4–8	2–3	0.378(5)	0.19(2)	0.975(8)	1.29

TABLE XIII. The same as in Table IX, but for $\beta = 3.2$.

R	t(SS)	t(SL)	M	$Y(\times 10^{-2})$	X	χ^2/d.o.f.
(S, B)	4–7	1–6	0.279(6)	0.518(11)	0.966(9)	1.74
(S, E)	4–7	1–4	0.278(5)	0.534(26)	0.965(9)	0.18
(PS)	3–9	3–6	0.439(8)	0.294(15)	0.932(9)	0.38
(E, B)	3–7	1–4	0.417(4)	0.062(4)	0.967(3)	2.77
(E, E)	3–7	1–3	0.415(4)	0.048(8)	0.965(3)	1.49
(T_2, B)	3–9	1–4	0.414(3)	0.0548(13)	0.959(4)	0.67
(T_2, E)	3–9	1–3	0.415(3)	0.033(5)	0.960(5)	0.67
(S, B)	4–7	1–8	0.282(5)	0.391(7)	0.968(7)	1.98
(S, E)	4–7	1–6	0.280(5)	0.376(11)	0.967(8)	0.31
(PS)	3–9	3–6	0.439(8)	0.299(15)	0.932(9)	0.40
(E, B)	3–7	1–3	0.415(4)	0.0693(23)	0.966(4)	3.29
(E, E)	3–7	1–3	0.416(4)	0.037(4)	0.965(4)	3.05
(T_2, B)	3–9	1–7	0.416(4)	0.068(2)	0.961(6)	0.96
(T_2, E)	3–9	1–3	0.415(3)	0.028(3)	0.960(4)	0.56
(T_2, B)	3–9	2–5	0.415(4)	0.068(3)	0.960(5)	0.74
(T_2, B)	3–9	1–3	0.415(3)	0.028(3)	0.960(4)	0.54

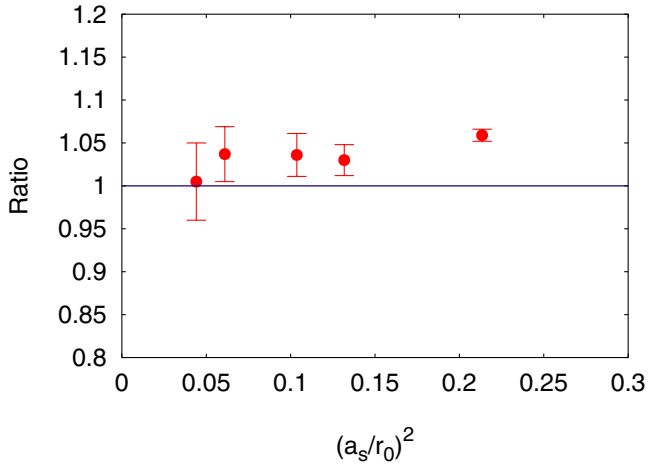

FIG. 11 (color online). The data points represent the ratios of the matrix elements of the two definitions of operator (T_2, B) at different lattice spacings. The straight line is plotted to show how far the ratios deviate from 1.

measured on lattice $L^3 \times T$. The results of $\delta_G(L)$ are shown in Fig. 12. In the figure, each point shows $\delta_G(L)$ of the matrix element of a glueball G, and the error bars come from the statistical errors of $f_G(L)$. The solid lines indicate $\delta_G = 0$, the dotted lines above and below the solid lines indicate $\delta_G = \pm 0.02$. The largest effects from the finite volume appear to occur in the Type-I operator of (E, B). All deviations are statistically consistent with zero, suggesting that systematic errors in these results from finite volume are no larger than the statistical errors. Since the physical volumes of the other β values are not smaller than the $8^3 \times 40$ at $\beta = 2.4$, we shall neglect the finite-volume effects for the higher β results.

TABLE XIV. The finite-volume effects of matrix elements at $\beta = 2.4$ and $\xi = 5$ on three different lattices $L^3 \times T = 16^3 \times 80$, $12^3 \times 64$, and $8^3 \times 40$. The fitted Y parameters are listed in normal numbers. For clarity, the Y parameters for lattice $L = 12$ and $L = 8$ are rescaled to $L = 16$ due to the relation $Y = \langle 0|O_L(0)|G\rangle/\sqrt{2M_G V}$ and illustrated by bold numbers. This table lists the Y parameters of Type-I operators.

	$L = 16$	$L = 12$	$L = 8$
(S, B)	**7.53(5)**	**7.50(5)**	**7.52(5)**
	7.53(5)	11.54(7)	21.27(15)
(S, E)	**7.38(12)**	**7.51(11)**	**7.47(8)**
	7.38(12)	11.56(17)	21.12(23)
(E, B)	**0.956(12)**	**0.993(8)**	**0.936(11)**
	0.956(12)	1.53(12)	2.64(3)
(E, E)	**0.56(5)**	**0.52(4)**	**0.54(3)**
	0.56(5)	0.81(6)	1.52(9)
(T_2, B)	**0.633(8)**	**0.649(8)**	**0.651(4)**
	0.633(8)	1.000(12)	1.841(11)
(T_2, E)	**0.29(2)**	**0.27(3)**	**0.30(2)**
	0.29(2)	0.42(4)	0.85(6)
(PS)	**1.85(4)**	**1.88(4)**	**1.85(4)**
	1.85(4)	2.89(6)	5.24(11)

TABLE XV. The same as Table XIV, but for Type-II operators.

	$L = 16$	$L = 12$	$L = 8$
(S, B)	**0.410(3)**	**0.408(3)**	**0.408(2)**
	4.10(3)	6.29(4)	11.54(6)
(S, E)	**5.73(6)**	**5.82(4)**	**0.579(4)**
	5.73(6)	8.97(6)	16.4(1)
(E, B)	**0.885(11)**	**0.895(9)**	**0.883(7)**
	0.885(11)	1.378(14)	2.50(2)
(E, E)	**47(2)**	**0.47(2)**	**0.48(2)**
	0.47(2)	0.72(3)	1.35(4)
(T_2, B)	**0.783(5)**	**0.792(4)**	**0.790(4)**
	0.783(5)	1.220(6)	2.24(1)
(T_2, E)	**0.25(2)**	**0.26(2)**	**0.26(2)**
	0.25(2)	0.40(3)	0.73(4)
(PS)	**1.87(4)**	**1.90(4)**	**1.89(4)**
	1.87(4)	2.92(6)	5.33(11)

Based on the discussions above, in the following continuum extrapolation of matrix elements, we use the results calculated on the lattice $8^3 \times 40$ at $\beta = 2.4$. As for the Type-II operators, we take the results with the lattice operators defined by $\hat{F}_{\mu\nu}(x)\hat{F}_{\rho\sigma}(x)$.

Using the fitted M and Y parameters listed in Table IX, X, XI, XII, and XIII, as well as the physical values of the lattice spacings a_s listed in Table V for each β, the lattice matrix elements $\langle 0|O_L|G\rangle$ can be obtained by $\langle 0|O_L|G\rangle = \sqrt{2M_G V}Y$. As a result, the matrix elements in units of r_0^{-3} are listed in Table XVII and illustrated by Fig. 13.

It is clear that the continuum limits can be extrapolated neither by the function with a single a_s^2 term nor with a single a_s^4 term. We fit them with the form

$$T(a_s)r_0^3 = T(0)r_0^3 + c_2\frac{a_s^2}{r_0^2} + c_4\frac{a_s^4}{r_0^4}, \qquad (37)$$

where T is the final nonrenormalized continuum-limit results of the glueball matrix elements.

Note that these matrix elements are all calculated by bare lattice operators. Before the renormalization of the

TABLE XVI. The same as Table XIV, but for the second definition of Type-II operators $O(T_2, B)$ and $O(T_2, E)$.

	$L = 16$	$L = 12$	$L = 8$
(T_2, E)	**0.825(6)**	**0.835(8)**	**0.837(4)**
	0.825(6)	1.285(12)	2.367(12)
(T_2, E)	**0.26(2)**	**0.26(2)**	**0.26(2)**
	0.26(2)	0.40(3)	0.73(4)

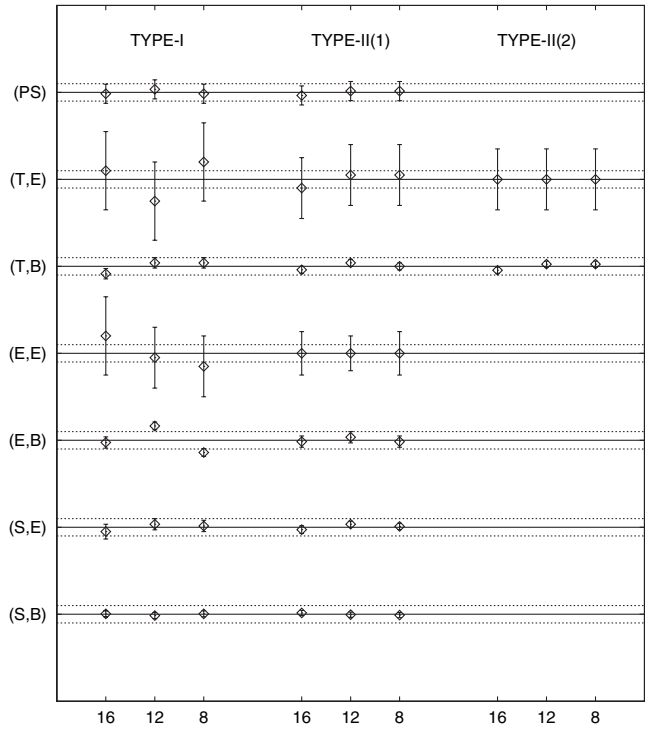

FIG. 12. Finite-volume effects on the results of the $\beta = 2.4$, $\xi = 5$ calculation. Each point shows the fractional change $\delta_G(L) = 1 - f_G(L)/\bar{f}_G$ in the matrix element of a glueball G, where $f_G(L)$ is the matrix element of G measured on the lattice $L^3 \times T$ with $L = 8$, 12, and 16, and $\bar{f}_G$ is the average value over those from different lattices. The errorbars come from the statistical errors of $f_G(L)$. The lattice labels L are shown along the horizontal axis, and the labels of different local operators are specified along the vertical axis. The solid lines indicate $\delta_G = 0$, the dotted lines above the solid lines indicate $\delta_G = 0.02$, and the dotted lines below the solid lines indicate $\delta_G = -0.02$. The FVE of different definitions of local operators are also shown in the figure.

local operators is performed, we cannot draw any conclusions of physical interest at present stage. However, we can give some comments on the different behaviors of the matrix elements of the Type-I and Type-II operators from the continuum extrapolation. Based on our experience from the calculation of glueball masses, the continuum $SO(3)$ symmetry is approximately restored for all the lattice spacings we use in this work, since the calculated glueball masses in T_2^{++} and E^{++} channel are coincident. The left panel of Fig. 13 is the plot of the matrix elements of the Type-I operators, where one can find that the calculated glueball matrix elements of T_2 and E irreps do not show this symmetry restoration. This is probably due to the definition of the Type-I operator introduced in Sec. II. The Type-I operators with different quantum number are defined by the real part of different Wilson loops composed of different numbers of spatial gauge links, such that the overall tadpole-improvement factors (different powers of the tadpole parameter u_s) are different for T_2 and E representation. The conjectured *power counting* of the tadpole parameter u_s for Wilson loops is a naive approximation and may bring additional deviation to the local operators. We have carried out the test that the naive tadpole parameters are replaced by the vacuum expectation value (VEV) of the corresponding Wilson loops. As we expected, the two matrix elements tend to coincide better. In contrast with the Type-I operators, all the Type-II operators are defined by the improved lattice version of the gauge strength tensor $\hat{F}_{\mu\nu}$ and thus have the same correction factor coming from the tadpole improvement. The right panel of Fig. 13 shows the behaviors of the matrix elements of the Type-II operators. It is clearly seen that the approximate $SO(3)$ symmetry restoration takes place for T_2 and E representation.

TABLE XVII. Final results of matrix elements of lattice gluonic operators. The data in the table are in the unit of r_0^{-3} with $r_0^{-1} = 0.410(20)$ MeV.

	$\beta = 2.4$ ($L = 8$)	$\beta = 2.6$ ($L = 12$)	$\beta = 2.7$ ($L = 12$)	$\beta = 3.0$ ($L = 16$)	$\beta = 3.2$ ($L = 24$)
$T(S, B)_I$	87(2)	90(2)	94(3)	92(3)	85(4)
$T(S, E)_I$	86(2)	89(4)	91(6)	90(6)	88(7)
$T(E, B)_I$	14.2(3)	12.5(5)	13.2(7)	12.6(8)	12.8(10)
$T(E, E)_I$	8.2(6)	6.8(10)	6.2(9)	7.9(12)	9.6(22)
$T(T_2, B)_I$	9.9(3)	9.8(4)	9.7(5)	9.8(7)	11.0(6)
$T(T_2, E)_I$	4.5(4)	4.1(6)	4.6(8)	4.3(7)	6.7(14)
$T(PS)_I$	30(1)	40(2)	46(3)	52(3)	61(5)
$T(S, B)_{II}$	47(1)	56(1)	60(2)	63(2)	64(3)
$T(S, E)_{II}$	67(2)	70(2)	71(4)	65(4)	62(4)
$T(E, B)_{II}$	13.4(4)	12.3(4)	13.6(5)	12.8(8)	13.8(9)
$T(E, E)_{II}$	7.3(3)	7.0(7)	6.2(6)	6.2(6)	7.4(10)
$T(T_2, B)_{II}$	12.7(3)	12.6(5)	13.0(7)	12.8(7)	13.6(9)
$T(T_2, E)_{II}$	3.9(3)	3.8(5)	4.4(5)	3.8(6)	5.6(10)
$T(PS)_{II}$	31(1)	40(2)	47(2)	53(3)	62(5)

The matrix elements of phenomenological interest, denoted s, p, and t, are defined as

$$\begin{aligned}(2\pi)^3\delta(\mathbf{0})\mathbf{s} &= \langle 0|\int d^3x S(x)|G\rangle,\\ (2\pi)^3\delta(\mathbf{0})\mathbf{p} &= \langle 0|\int d^3x P(x)|G\rangle,\\ (2\pi)^3\delta(\mathbf{0})\mathbf{t}\boldsymbol{\epsilon}_{\mu\nu} &= \langle 0|\int d^3x \Theta(x)|G\rangle,\end{aligned} \tag{38}$$

where $\boldsymbol{\epsilon}_{\mu\nu} = \boldsymbol{\epsilon}_{\nu\mu}$, $\boldsymbol{\epsilon}_{\mu\mu} = 0$, $\boldsymbol{\epsilon}_{\mu\nu}\boldsymbol{\epsilon}_{\mu\nu} = 1$, and $S(x)$, $P(x)$, $\Theta_{\mu\nu}(x)$ are defined in Eq. (1) and Eq. (3). Recalling that $(2\pi)^3\delta(\mathbf{0})$ is replaced by $L^3a_s^3$ on finite lattices, and combining Eq. (7)–(11), s, p, and t can be reproduced by the calculated matrix elements listed in Table XVII as

$$\begin{aligned}sr_0^3 &= 2(T(S, B) + T(S, E)),\\ pr_0^3 &= 8T(PS),\\ t_E r_0^3 &= 2|T(E, B) - T(E, E)|,\\ t_{T_2} r_0^3 &= 2|T(T_2, B) - T(T_2, E)|.\end{aligned} \tag{39}$$

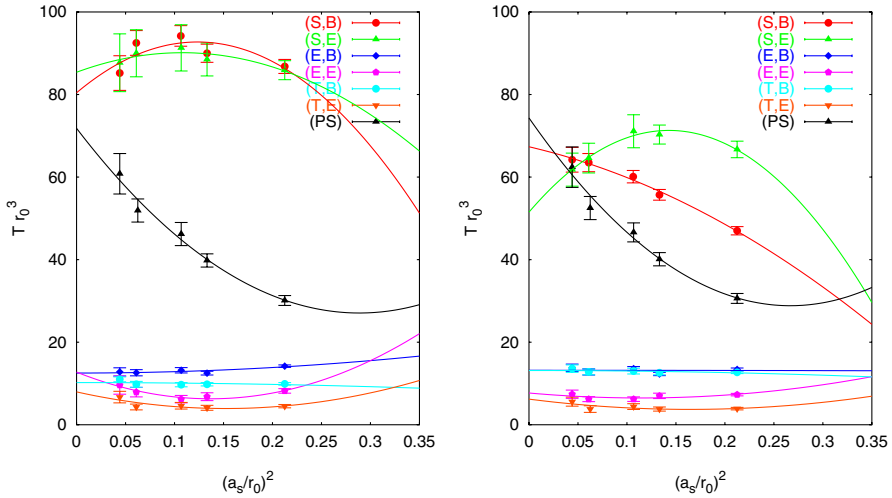

FIG. 13 (color online). Glueball matrix elements (ME) in terms of r_0^3 against the lattice spacing square $(a_s/r_0)^2$. The calculated values of ME's are plotted in points, with different colors corresponding to different channels. The curves are best fits to the calculated results by the model $T(a_s)r_0^3 = T(0)r_0^3 + c_2(a_s/r_0)^2 + c_4(a_s/r_0)^4$. The left panel illustrates the result of Type-I operators, while the right panel is for Type-II operators.

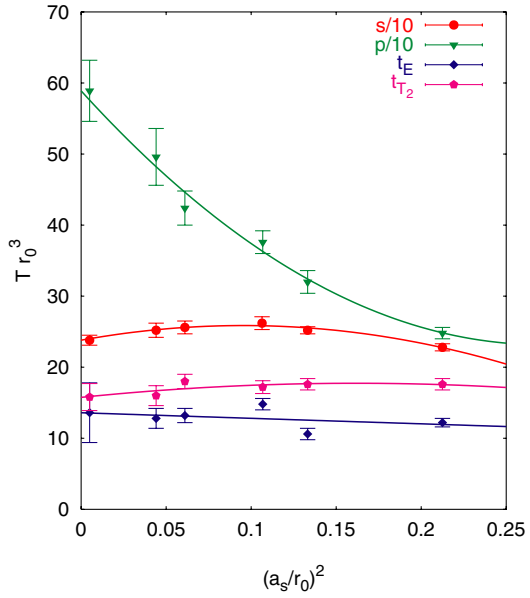

FIG. 14 (color online). The nonrenormalized matrix elements s, p, and t from Type-II operators are plotted versus lattice spacing. The continuum extrapolations are also carried out.

Figure 14 and Table XVIII illustrate the behaviors of these matrix elements with respect to the lattice spacings. We only show the data reproduced from the Type-II operators, which can be only renormalized in this work (see Section V). The continuum limits of t_{T_2} and t_E are consistent within error bars. The deviation of the central values comes mainly from the discrepancy of $T(E, E)$ and $T(T_2, E)$.

IV. THE NONPERTURBATIVE RENORMALIZATION OF LOCAL GLUONIC OPERATORS

The lattice local gluonic operator O and its continuum counterpart O_{cont} is related by the renormalization constant $Z_O(a)$,

$$O_{\text{cont}} = a^{-4} Z_O(a) O. \tag{40}$$

The key question is to choose a proper normalization condition, so that the renormalization constant can be determined. In this work, we choose the energy-momentum tensor in the glueball state as the normalization condition [11].

TABLE XVIII. The nonrenormalized matrix elements s, p, and t in units of r_0^{-3} are reproduced from the lattice results of Type-II operators at different lattice spacings. The errors quoted here are purely statistical. The continuum limits are also listed for each channel.

	$\beta = 2.4$	$\beta = 2.6$	$\beta = 2.7$	$\beta = 3.0$	$\beta = 3.2$	Continuum
sr_0^3	228(5)	252(5)	262(9)	256(9)	252(10)	227(7)
pr_0^3	248(8)	320(16)	376(16)	424(24)	496(40)	589(43)
$t_E r_0^3$	12.2(5)	10.6(8)	14.8(8)	13.2(1.0)	12.8(1.4)	13.6(4.1)
$t_{T_2} r_0^3$	17.6(0.8)	17.6(0.8)	17.2(0.9)	18.0(1.0)	16.0(1.4)	15.8(1.9)

The energy-momentum tensor for the pure gauge theory

$$\bar{T}_{\mu\nu} = \bar{T}_{\nu\mu} = -\frac{1}{2}\delta_{\mu\nu}\mathrm{Tr}F^2 + 2\mathrm{Tr}F_{\mu\alpha}F_{\nu\alpha} \tag{41}$$

satisfies $\partial_\mu \bar{T}_{\mu\nu} = 0$ and does not need an overall renormalization in the continuum. More specifically, $\bar{T}_{00} = Tr(\mathbf{E}^2 - \mathbf{B}^2))$. At the classical level, $\bar{T}_{\mu\nu}$ is traceless. When quantum corrections are included, the renormalized energy-momentum tensor, $T_{\mu\nu}$, takes a nonvanishing trace part, $\hat{T}_{\mu\nu}$, which comes from the anomalous breaking of scale invariance and is called the QCD trace anomaly,

$$\hat{T}_{\mu\nu} = -\frac{1}{4}\frac{\beta(g)}{2g}\delta_{\mu\nu}F^2 = \frac{11}{32\pi^2}\delta_{\mu\nu}Tr(g^2\mathbf{B}^2 + g^2\mathbf{E}^2), \tag{42}$$

where $\beta(g) = -\beta_0 g^3/(4\pi)^2$ is the β function of QCD to the lowest order of the coupling constant g with $\beta_0 = 11$ in the pure gauge case. Thus, $T_{\mu\nu}$ can be written explicitly as the sum of the traceless and trace parts,

$$T_{\mu\nu} = \bar{T}_{\mu\nu} + \hat{T}_{\mu\nu}. \tag{43}$$

On the other hand, $T_{\mu\nu}$ defines the Hamiltonian operator of the theory

$$H = \int d^3x T_{00}(\mathbf{x}, 0), \tag{44}$$

which is finite and scale independent. In the rest frame of a glueball, the matrix element of the Hamiltonian H in the glueball state is just the glueball's rest mass,

$$M_G = \frac{\langle G(M_G, \mathbf{p} = 0)|\int d^3x T_{00}(\mathbf{x}, 0)|G(M_G, \mathbf{p} = 0)\rangle}{\langle G|G\rangle}. \tag{45}$$

If the glueball states $|G(E, \mathbf{p})\rangle$ are normalized as

$$\langle G(E_p, \mathbf{p})|G(E_p, \mathbf{p}')\rangle = 2E_p(2\pi)^3\delta^3(\mathbf{p} - \mathbf{p}'), \tag{46}$$

we have $\langle G(M_G, \mathbf{p} = 0)|\int d^3x T_{00}(\mathbf{x}, 0)|G(M_G, \mathbf{p} = 0)\rangle = 2M_G^2(2\pi)^3\delta^3(\mathbf{0}) \equiv 2p^0p^0(2\pi)^3\delta^3(\mathbf{0})$, which implies that

$$\langle G(p)|\int d^3x T_{\mu\nu}(\mathbf{x}, 0)|G(p)\rangle = 2p^\mu p^\nu(2\pi)^3\delta^3(\mathbf{0}). \tag{47}$$

Combining Eq. (45) and (47), we get the normalization conditions in the glueball's rest frame,

$$\begin{aligned}\langle G(p)|\int d^3x\bar{T}_{\mu\nu}(\mathbf{x}, 0)|G(p)\rangle &= 2(p^\mu p^\nu - \tfrac{1}{4}M_G^2\delta_{\mu\nu}) \\ &\quad\times(2\pi)^3\delta^3(\mathbf{0}), \\ \langle G(p)|\int d^3x\hat{T}_{\mu\nu}(\mathbf{x}, 0)|G(p)\rangle &= \tfrac{1}{2}M_G^2\delta_{\mu\nu}(2\pi)^3\delta^3(\mathbf{0}).\end{aligned} \tag{48}$$

According to the definitions in Eq. (9) and Eq. (10), the E and T_2 operators are related to $\bar{T}_{ij}$ by

$$\begin{aligned}O_1^{(E,E)} - O_1^{(E,B)} &\propto \bar{T}_{11} - \bar{T}_{22}, \\ O_2^{(E,E)} - O_2^{(E,B)} &\propto 2\bar{T}_{33} - \bar{T}_{11} - \bar{T}_{22}, \\ O_i^{(T_2,E)} - O_i^{(T_2,B)} &\propto \epsilon_{ijk}\bar{T}_{jk},\end{aligned} \tag{49}$$

whose matrix elements in a zero-momentum glueball state vanish, thus we cannot renormalize E^{++} and T_2^{++} operators directly by the normalization condition in Eq. (48) in the glueball rest frame. A possible way around this difficulty is to assume the almost restoration of Lorentz invariance at the lattice spacings we use in this work, so the overall renormalization constant of the lattice version of $\bar{T}_{\mu\nu}$ can be determined by one of its components. In fact, this is justified to some extent by two facts. First, it is argued that the rotational invariance can be restored if the scale parameter $z = m_{A_1^{++}}L$ is larger than 10 [12], and our smallest lattice gives the value $z = 0.31 \times 5 \times 8 = 12.4$ which meets this requirement. Secondly, in our lattice calculations of the mass spectrum and matrix elements, the coincidence of E^{++} channel and T_2^{++} channel implies that this rotational restoration is actually realized. Based on the discussion above, we choose the component $\bar{T}_{00}$ to do the renormalization of the tensor operator in this work. In the practical study, we calculate the matrix elements $\langle G|O_\pm|G\rangle_{\mathrm{lat}}$, where $O_\pm$ is the operator $g^2Tr(\mathbf{E}^2 \pm \mathbf{B}^2)$ and $|G\rangle = |A_1^{++}\rangle$, $|E^{++}\rangle$, or $|T_2^{++}\rangle$. As we have addressed before, O_- is proportional to $\bar{T}_{00}$, and O_+ is proportional to the trace anomaly $\hat{T}_{00}$. Thus, the renormalization constants of the scalar and tensor operators can be extracted from these matrix elements.

The matrix elements $\langle G|O_\pm|G\rangle_{\mathrm{lat}}$ can be obtained by calculating the three-point function

$$\begin{aligned}C_3(t_1, t_2) &= \langle 0|O_s(-t_1)O_\pm(0)O_s(t_2)|0\rangle = \sum_{m,n}\frac{1}{4E_nE_mV^2}\langle 0|O_S(-t_1)|n\rangle\langle n|O_\pm(0)|m\rangle\langle m|O_S(t_2)|0\rangle \\ &= \sum_{m,n}\frac{1}{4E_nE_mV^2}\langle 0|O_S(0)|n\rangle\langle n|O_\pm(0)|m\rangle\langle m|O_S(0)|0\rangle e^{-E_nt_1}e^{-E_mt_2} \\ &\to \frac{1}{(2M_GV)^2}\langle 0|O_s(0)|G\rangle|^2\langle G|O_\pm(0)|G\rangle e^{-M_G(t_1+t_2)}(t_1, t_2 \to \infty),\end{aligned} \tag{50}$$

where $O_S(t)$ is the smeared zero-momentum operator which generates the ground state $|G\rangle$ from the vacuum, and M_G the ground state mass. Using the asymptotic form of the two-point function

$$C_{SS}(t) \sim \frac{1}{2M_G V}|\langle 0|O_S(0)|G\rangle|^2 e^{-M_G t}(t \to \infty) \tag{51}$$

and dividing the three-point function by proper two-point function, one gets

$$\frac{C_3(t_1, t_2)}{C_{SS}(t_1)} \approx \frac{1}{2M_G V}\langle G|O_{\pm}(0)|G\rangle e^{-M_G t_2}(t_1, t_2 \to \infty). \tag{52}$$

In the practical data processing, by analogy with the extraction of the matrix element, we fit $C_2(t)$ and $C_3(t, t_0)$ simultaneously with the fitting model

$$C_{SS}(t) = X^2 e^{-Mt} C_3(t, t_0) = X^2 W e^{-M(t+t_0)}, \tag{53}$$

where $t_0 = 1$. W is related to the matrix element $\langle G|O_{\pm}(0)|G\rangle$ by

$$\langle G|O_{\pm}(0)|G\rangle = 2M_G V W. \tag{54}$$

From Eq. (40), Eq. (48), and the fitted matrix elements $\langle G|O_{\pm}|G\rangle_{\text{lat}}$, the renormalization constants for scalar and tensor gluonic operators can be derived as

$$\begin{aligned} \frac{1}{Z_S(a_s)} &= \frac{11}{32\pi^2}\frac{2}{M_G^2 a_s^4}\langle G|O_+|G\rangle_{\text{lat}}, \\ \frac{1}{Z_T(a_s)} &= \frac{1}{g^2}\frac{2}{3M_G^2 a_s^4}\langle G|O_-|G\rangle_{\text{lat}}, \end{aligned} \tag{55}$$

where the coupling constant g^2 comes from the relation $\bar{T}_{00} = (1/g^2)O_-$.

Unfortunately, the gluonic three-point function is far more noisy than the gluonic two-point function in Monte Carlo calculation. In this work, the renormalization of gluonic operators is performed only at $\beta = 2.4$ on the lattice $8^3 \times 40$ with $\xi = 5$. As many as 100 000 measurements are carried out, the signals of three-point functions are still weak with large fluctuation. In the practical computation, the matrix elements of Type-I and Type-II operators of $O^{(S,B)}$ and $O^{(S,E)}$ are all calculated. It is found that the three-point functions involving Type-I operators are so noisy that the matrix elements cannot be extracted reliably. The three-point functions involving Type-II operators behave better, from which we obtain the renormalization constants. The matrix elements $\langle G|O_{\pm}|G\rangle_{\text{lat}}$ and the resultant renormalization constants at $\beta = 2.4$ are listed in Table XIX.

As for the renormalization of the pseudoscalar operator, we shall use the quenched topological susceptibility χ as the normalization condition. The quantity χ is defined by

$$\chi = \int d^4x \langle q(x)q(0)\rangle, \tag{56}$$

where the topological charge density $q(x)$ is proportional to the pseudoscalar operator $P(x)$ (defined in Eq. (1)) as $q(x) = \frac{1}{32\pi^2}P(x)$. While there are many lattice calculations of χ, we regard the most recent work [13] where the topological charge is defined through Neuberger's overlap operator [14] to be most reliable. With controlled systematics, the value at the continuum is reported to be $\chi = (191 \pm 5\ \text{MeV})^4$ which is close to the phenomenological value of $(180\ \text{MeV})^4$ from the Witten-Veneziano mass formula for the η' measured mass [15,16].

Our lattice version of χ, denoted by χ_L, is defined by the lattice pseudoscalar operator $O(PS)(x)$ as

$$\chi_L = \frac{\xi}{(32\pi^2)^2 L^3 T a_s^4}\sum_{x,y}\langle O^{(PS)}(x)O^{(PS)}(y)\rangle, \tag{57}$$

TABLE XIX. The matrix elements of operator $O_{\pm}$ (Type-II) in glueball states are listed. S represents the scalar glueball state, while $T(E)$ and $T(T_2)$ denote the tensor glueballs in E and T_2 irreps, respectively. The renormalization constants extracted from these matrix elements are given also.

$\|G\rangle$	$\langle G\|O_+\|G\rangle_{\text{lat}}$	Z_S	$\langle G\|O_-\|G\rangle_{\text{lat}}$	Z_T
S	32(9)	1.1(3)	13(5)	0.7(3)
$T(E)$	102(16)	1.0(2)	51(15)	0.53(15)
$T(T_2)$	101(16)	1.0(2)	53(15)	0.51(15)

TABLE XX. The nonrenormalized topological susceptibility $\chi_L(a_s)$ calculated at different lattice spacing are listed in physical units. Also listed are the ratios of $\chi_L^{1/2}(a_s)$ and the nonrenormalized matrix elements of pseudoscalar $p(a_s)$ after rescaled by their continuum extrapolation values $\chi_L^{1/2}(0)$ and $p(0)$.

β	2.4	2.6	2.7	3.0	3.2	Continuum
$\chi_L^{1/4}(a_s)$ (MeV)	242(4)	277(5)	299(5)	323(6)	351(8)	391(15)
$p(a_s)r_0^3$	248(8)	320(16)	376(16)	424(24)	496(40)	589(43)
$\frac{p(a_s)\chi_L^{1/2}(0)}{\chi_L^{1/2}(a_s)p(0)}$	1.10(7)	1.08(9)	1.09(8)	1.06(10)	1.05(11)	1.00(13)

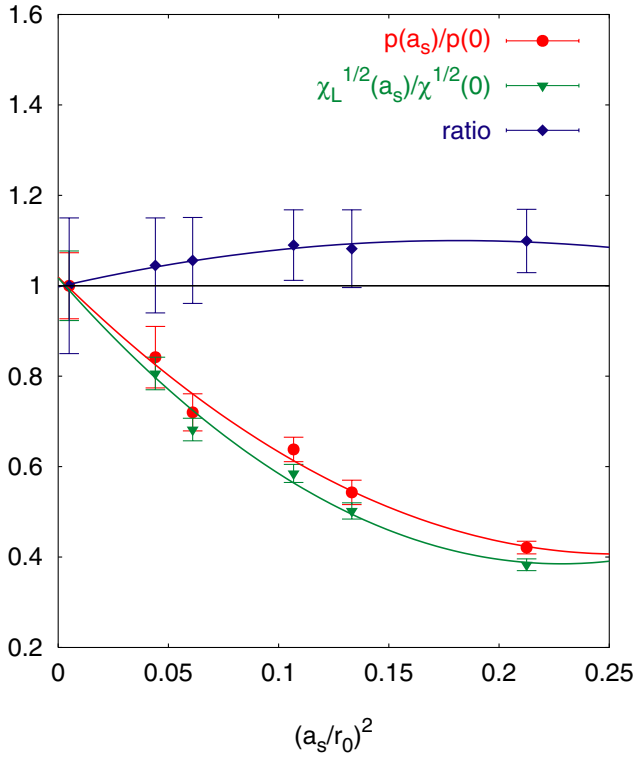

FIG. 15 (color online). The a_s-dependences of $\chi_L^{1/2}(a_s)$ and $p(a_s)$ are plotted. For comparison, $\chi_L^{1/2}(a_s)$ and $p(a_s)$ are rescaled by their continuum-extrapolated values, say, $\chi_L^{1/2}(0)$ and $p(0)$, respectively. One can find that the a_s-dependences of $\chi_L^{1/2}(a_s)$ and $pr_0^3(a_s)$ are very similar and their ratios are fairly constant.

where L and T are the lattice sizes in spatial and temporal directions, respectively.

We have calculated $\chi_L(a_s)$ for all the five β, at each β 20 000 measurements are carried out. In Table XX are listed the results of $\chi_L^{1/4}(a_s)$ in units of MeV for different β, as well as the nonrenormalized continuum value $\chi_L^{1/4}(0)$ after the continuum extrapolation $a_s \to 0$. It is obvious that the value of $\chi_L^{1/4}(a_s)$ increases along with the decreasing of lattice spacing. For comparison, the nonrenormalized matrix elements $pr_0^3(a_s)$ at different β's are also listed in Table XX. In Fig. 15 are plotted the a_s-dependences of $\chi_L^{1/2}(a_s)$ and $pr_0^3(a_s)$ (rescaled by their continuum-extrapolated values, respectively), as well as their ratios, where one can find that the a_s-dependences of $\chi_L^{1/2}(a_s)$ and $pr_0^3(a_s)$ are very similar and their ratios are fairly constant. Using $\chi^{1/4} = 191$ MeV, the renormalization constant Z_P of pseudoscalar operator in the continuum limit can be extracted as

$$Z_P^{-1} = \frac{\chi^{1/2}}{\chi_L^{1/2}(0)} \approx 0.24(2). \tag{58}$$

V. RESULTS AND DISCUSSION

After the continuum extrapolation and the renormalization of the local operators, we can discuss the physical implication of our lattice results.

As we addressed above, we have tried to extract the renormalization constants for scalar and tensor operator only at $\beta = 2.4$. In fact, the signals of the three-point functions of Type-I operator are very poor, so the renormalization constants Z_S and Z_T are obtained only for Type-II operators. We are lucky with this situation because all the Type-II operators are made up of the lattice version of the gauge field strength, $\hat{F}_{\mu\nu}$, thus they all have the same normalization constant, say, the same tadpole-improvement factor. Therefore, for Type-II operator, the Z_T extracted from $\bar{T}_{00}$ can be applied to other components involved in the glueball matrix elements calculated in this work.

Considering Eq. (3) and (6), the nonrenormalized matrix elements of the $S(x)$, $P(x)$, and $\Theta(x)$ in the continuum can be obtained by the lattice results, and are shown in Table XVIII. We notice that, although the (S, B) and (S, E) matrix elements have sizeable a_s dependence for the Type-II operator, as seen in Fig. 13, the total scalar matrix element, which is the sum of the two, is much flatter in $(a_s/r_0)^2$. This is also the case for the tensor matrix element. With the observation that the nonrenormalized matrix elements of the scalar and the tensor depend on the lattice spacing $(a_s/r_0)^2$ very mildly, we speculate that there is not a large lattice spacing dependence in the renormalization constant, and will use Z_S and Z_T computed at $\beta = 2.4$ as an approximation of the renormalization constants in the continuum limit. We shall check this in the future when computer resources are available for high statistics calculation at larger β.

Taking the average of the renormalization constant Z_S from Table XIX, we get a continuum-extrapolated value for the matrix element $\langle 0|S|0^{++}\rangle = 15.6 \pm 3.2$ GeV^3. Based on the scaling properties of QCD and trace anomaly, both the QCD sum rule [17] and the soft meson theorem [18] lead to an estimate that relates the scalar glueball matrix element to the gluon condensate,

$$\langle 0|S|0^{++}\rangle = 16\pi^2\sqrt{\frac{G_0}{2b}}M_G, \tag{59}$$

where $G_0 = \langle 0|\frac{\alpha_s}{\pi}G^a_{\mu\nu}G^a_{\mu\nu}|0\rangle$ is the gluon condensate, $b = (11/3)N_c - (2/3)N_f$ and M_G the scalar glueball mass. Taking $N_f = 0$, $G_0 = 0.012$ GeV^4, and $M_G \approx 1.7$ GeV, this matrix element is estimated to be $\sim$6.3 GeV, which is about two and a half times smaller than our lattice result. This discrepancy might be attributable to the fact that the quenched lattice calculation gives a gluon condensate which is about 0.14 ± 0.02 GeV^4 [19]. This is larger by an order of magnitude than that used in QCD sum rule. If the relation Eq. (59) still holds in the pure

gauge theory, using the quenched gluon condensate, the estimated scalar matrix element is estimated to be (21 ± 1) GeV^3 which is in good agreement with our quenched lattice calculation.

For the pseudoscalar, with the renormalization constant $Z_P^{-1} = 0.24(2)$ determined in the last section, the lattice calculation gives the result $\langle 0|P|0^{-+}\rangle \approx 9.7 \pm 1.5$ GeV^3. It has been proposed that there is an approximate chiral symmetry between the scalar and pseudoscalar glueballs [20]. A sum rule is derived from an effective action which relates the topological susceptibility χ in the pure gauge case to the gluon condensate G_0,

$$\chi = \eta^{-2}\sqrt{\frac{G_0}{2b}}, \tag{60}$$

where $\eta \approx 0.7$. Using our lattice results, the degree of chiral symmetry η can be obtained from the ratio of the pseudoscalar to scalar matrix elements [20], $\eta_L = \langle 0|P|0^{-+}\rangle/(2\langle 0|S|0^{++}\rangle) \approx 0.3$, which is also more than 2 times smaller than the result of QCD sum rule. These facts hint that there may be a substantial quenching effect in the matrix element of the scalar.

We can also estimate the glueball contribution to the topological susceptibility by the lattice matrix element and glueball mass,

$$\chi_{\text{glueball}} = \left(\frac{\langle 0|P|0^{-+}\rangle}{32\pi^2 M_{0^{-+}}}\right)^2 \approx (110 \text{ MeV})^4 \sim 0.11\chi, \tag{61}$$

which implies that the pseudoscalar glueball gives an appreciable 11% contribution to the topological susceptibility.

In the tensor channel, the glueball matrix element is extrapolated to 1.0 ± 0.2 GeV^3 in the continuum, which is the average of results of E and T_2 channels. In the calculation, it is found that in the lattice spacing range we use, the glueball mass and matrix elements are approximately independent of the lattice spacing, this implies that the lattice artifacts might be neglected here. If the renormalization constant $Z_T \approx 0.52(15)$ of the tensor operator does not change much in the range of lattice spacing and applies to all the β values in this work, the renormalized matrix element of tensor operator is 0.52 ± 0.19 GeV^3, which is in agreement with the prediction 0.35 GeV^3 from the tensor dominance model [21] and QCD sum rule [22] for the tensor mass around 2.2 GeV.

VI. CONCLUSION

The glueball mass spectrum and glueball-to-vacuum matrix elements are calculated on anisotropic lattices in this work. The calculations are carried out at five lattice spacings a_s's which range from 0.22 fm to 0.10 fm. Because of the implementation of the improved gauge action and improved gluonic local operators, the lattice artifacts are highly reduced. The finite-volume effects are carefully studied with the result that they can be neglected on the lattices we used in this work.

As to the glueball spectrum, we have carried out calculations similar to the previous work [4] on much larger and finer lattices, so that the liability of the continuum-limit extrapolation is reinforced. Our results of the glueball spectrum are summarized in Table XXI and Fig. 16.

After the nonperturbative renormalization of the local gluonic operators, we finally get the matrix elements of

TABLE XXI. The final glueball spectrum in physical units. In column 2, the first error is the statistical uncertainty coming from the continuum extrapolation, the second one is the 1% uncertainty resulting from the approximate anisotropy. In column 3, the first error comes from the combined uncertainty of $r_0 M_G$, the second from the uncertainty of $r_0^{-1} = 410(20)$ MeV.

J^{PC}	$r_0 M_G$	M_G (MeV))
0^{++}	4.16(11)(4)	1710(50)(80)
2^{++}	5.83(5)(6)	2390(30)(120)
0^{-+}	6.25(6)(6)	2560(35)(120)
1^{+-}	7.27(4)(7)	2980(30)(140)
2^{-+}	7.42(7)(7)	3040(40)(150)
3^{+-}	8.79(3)(9)	3600(40)(170)
3^{++}	8.94(6)(9)	3670(50)(180)
1^{--}	9.34(4)(9)	3830(40)(190)
2^{--}	9.77(4)(10)	4010(45)(200)
3^{--}	10.25(4))(10)	4200(45)(200)
2^{+-}	10.32(7)(10)	4230(50)(200)
0^{+-}	11.66(7)(12)	4780(60)(230)

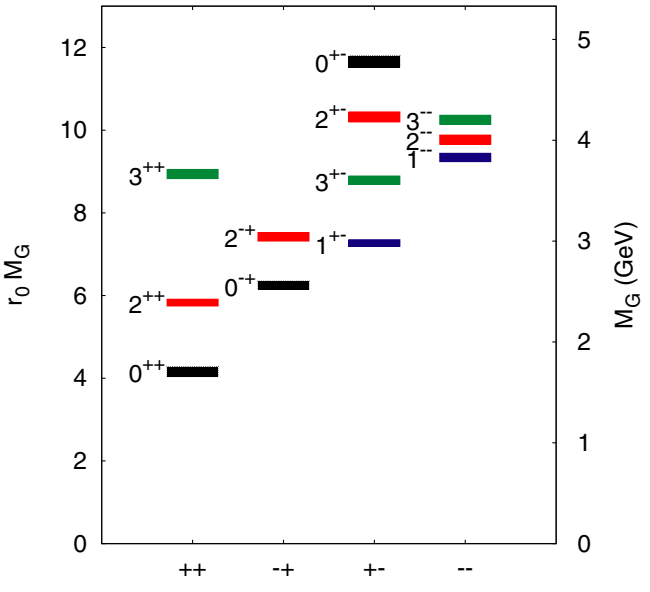

FIG. 16 (color online). The mass spectrum of glueballs in the pure $SU(3)$ gauge theory. The masses are given both in terms of r_0 ($r_0^{-1} = 410$ MeV) and in GeV. The height of each colored box indicates the statistical uncertainty of the mass.

scalar (s), pseudoscalar (p), and tensor operator (t) with the results

$$\begin{aligned} s &= 15.6 \pm 3.2\ (\mathrm{GeV})^3, \\ p &= 9.7 \pm 1.5\ (\mathrm{GeV})^3, \\ t &= 0.52 \pm 0.19\ (\mathrm{GeV})^3, \end{aligned} \tag{62}$$

where the errors of s and t come mainly from the errors of the renormalization constants Z_S and Z_T. The more precise calculation of Z_S and Z_T will be carried out in later work.

ACKNOWLEDGMENTS

This work is supported in part by U.S. Department of Energy under Grants No. DE-FG05-84ER40154 and No. DE-FG02-95ER40907. The computing resources at NERSC (operated by DOE under No. DE-AC03-76SF00098) and SCCAS (Deepcomp 6800) are also acknowledged. Y. Chen and S. J. Dong are partly supported by NSFC (No. 10075051, No. 10235040) and CAS (No. KJCX2-SW-N02). C. Morningstar is also supported by NSF under Grant No. PHY-0354982.

[1] B. Berg and A. Billoire, Nucl. Phys. **B221**, 109 (1983).
[2] G. Bali, *et al.* (UKQCD Collaboration), Phys. Lett. B **309**, 378 (1993).
[3] C. Michael and M. Teper, Nucl. Phys. **B314**, 347 (1989).
[4] C. Morningstar and M. Peardon, Phys. Rev. D **56**, 4043 (1997); Phys. Rev. D **60**, 034509 (1999).
[5] K. F. Liu, in *Hadron Spectroscopy*, edited by S. Oneda, AIP Conf. Proc. No. 132 (AIP, New York, 1985), p. 485.
[6] Y. Liang, K. F. Liu, B. A. Li, and K. Ishikawa, Nucl. Phys. B, Proc. Suppl. **20**, 189 (1991).
[7] Y. Liang, K. F. Liu, B. A. Li, S. J. Dong, and K. Ishikawa, Phys. Lett. B **307**, 375 (1993).
[8] G. P. Lepage and P. B. Mackenzie, Phys. Rev. D **48**, 2250 (1993).
[9] Yu. A. Simonov, Yad. Fiz. **50**, 213 (1989) [Sov. J. Nucl. Phys. **50**, 134 (1989).
[10] R. Sommer, Nucl. Phys. **B411**, 839 (1994).
[11] X. Ji, Phys. Rev. Lett. **74**, 1071 (1995).
[12] M. Lüscher, Phys. Lett. **118B**, 387 (1982).
[13] L. D. Debbio, L. Giusti, and C. Pica, Phys. Rev. Lett. **94**, 032003 (2005).
[14] H. Neuberger, Phys. Lett. B **417**, 141 (1998).
[15] E. Witten, Nucl. Phys. **B156**, 269 (1979).
[16] G. Veneziano, Nucl. Phys. **B159**, 213 (1979).
[17] V. A. Novikov, M. A. Shifman, A. I. Vainshtein, and Zakharov, Nucl. Phys. **B165**, 67 (1980).
[18] J. Ellis and J. Lanik, Phys. Lett. **150B**, 289 (1985).
[19] A. Di. Giacomo, H. G. Dosch, V. I. Shevchenko, and Yu. A. Simonov, Phys. Rep. **372**, 319 (2002).
[20] J. M. Cornwall and A. Soni, Phys. Rev. D **29**, 1424 (1984).
[21] K. Ishikawa, I. Tanaka, K. F. Liu, and B. A. Li, Phys. Rev. D **37**, 3216 (1988).
[22] S. Narison, Z. Phys. C **26**, 209 (1984).